

Student thesis series INES nr 321

# **Posidonia Oceanica habitat mapping in shallow coastal waters along Losinj Island, Croatia using Geoeye-1 multispectral imagery**

***Sam Khallaghi***

2014

Department of

Physical Geography and Ecosystems Science

Lund University

Sölvegatan 12

S-223 62 Lund

Sweden



Sam Khallaghi (2014). Posidonia Oceanica habitat mapping in shallow coastal waters along Losinj Island, Croatia using Geoeye-1 multispectral imagery.

Master degree thesis, 30 credits in Geomatics

Department of Physical Geography and Ecosystems Science,

Lund University

Level: Master of Science (MSc)

Course duration: *January 2012 until June 2014*

#### Disclaimer

This document describes work undertaken as part of a program of study at the University of Lund. All views and opinions expressed herein remain the sole responsibility of the author, and do not necessarily represent those of the institute.

**Sam Khallaghi**

***Master thesis, 30 credits, in Geomatics***

*Supervisors:*

**Ulrik Mårtensson**

**Luka Traven**

*Department of Physical Geography and Ecosystem Science*

*Lund University*

*February 2014*

## **Abstract**

The wide coverage and periodic nature of remote sensing satellites made them a useful tool in coastal management during the last two decades. Seagrass species are a powerful indicator of the marine environment condition and a main source of primary production in both marine and fresh water ecosystems. In this thesis, a study was carried out using Geoeye-1 satellite data acquired on July and August 2011 to extract bottom type features, i.e. seagrass (*Posidonia Oceanica*), sand and rock in shallow coastal waters of Losinj Island, Croatia.

Prior to classification, atmospheric impacts have been removed using the ATCOR atmospheric module in ERDAS imagine 2011. But due to quality problems the glint correction using Hedley's method and elimination of the water column effects using Lyzenga's method to produce depth invariant indices for each band pairs was unsuccessful. To improve the spectral distinction of bottom features a combination of PCI and visible bands were used to form the basis of Maximum likelihood classification. Also to compensate the water column problem, training areas for each main class were considered as separate individual classes and then get aggregated to make the parent class. Efficiency of the classification was evaluated by assessing the accuracy of the generated thematic maps which showed a satisfactory result for the total accuracy of the classified images.

## **Acknowledgment**

I would like to express my special appreciation and thanks to my advisor Ulrik Mårtensson, you have been a tremendous mentor for me. I would like to thank you for encouraging my research and for allowing me to grow as a research scientist. Your advice on both research as well as on my career have been priceless. Furthermore I would like to thank Professor Petter Pilesjö for introducing me to the topic as well for the support on the way. Also, I like to thank my second supervisor Luka Traven and all the other participants in the survey, who have willingly shared their precious time during the process of field work sampling. A special thanks to my family. Words cannot express how grateful I am to my mother and father for all of the sacrifices that you've made on my behalf. At the end I would like express appreciation to my beloved fiancée, Mona who spent sleepless nights with me and always showed her support in the moments when there was no one to answer my queries.

# Table of Contents

Abstract .....	I
Acknowledgment .....	II
Table of Contents .....	III
List of figures and tables .....	V
Abbreviations .....	VI
<b>Chapter 1: Introduction</b> .....	<b>1</b>
1.1 General background on seagrass .....	1
1.2 The importance of seagrass .....	1
1.3 Seagrass threats .....	2
1.4 Research problem: A remote sensing perspective .....	2
1.5 Research Objectives .....	3
1.5.1 Specific objective.....	3
1.5.2 Research question.....	3
1.6 Study area .....	3
1.7 data sources .....	6
1.7.1 Geoeye-1 satellite imagery .....	6
1.7.2 Field work.....	8
1.8 software .....	8
1.8.1 ENVI.....	8
1.8.2 ERDAS IMAGINE .....	8
1.9 Organization of the research.....	9
<b>Chapter 2 – Theoretic background of the methods</b> .....	<b>10</b>
2.1 Interaction of light with water body and atmosphere.....	10
2.2 Atmospheric correction.....	12
2.2.1 Radiance to reflectance conversion.....	12
2.2.2 Relative atmospheric correction methods.....	14
2.2.3 Absolute atmospheric correction methods .....	14
2.3 Sun glint correction .....	15
2.4 Water column correction .....	16
2.5 Principle Component Analysis (PCA).....	20
2.6 Classification.....	21
2.6.1 Post-classification.....	22
2.7 Accuracy assessment.....	23
2.8 Previous works .....	23
<b>Chapter 3 – Implementation and result</b> .....	<b>26</b>
3.1 Image processing overview .....	26
3.2 method one.....	26
3.2.1 Atmospheric correction .....	26
3.2.2.1 FLAASH .....	26

3.2.2.2 ATCOR.....	28
3.2.2 Masking .....	29
3.2.3 Sun glint removal .....	33
3.2.4 Water column correction .....	34
3.3 Method two.....	36
3.3.1 Principle component analysis.....	36
3.3.2 Classification .....	37
3.3.3 Post classification .....	42
<b>Chapter 4 – Discussion and conclusion</b> .....	<b>43</b>
4.1 Discussion.....	43
4.2 Conclusion and future work.....	46
<b>References</b> .....	<b>48</b>
Appendix A- Metadata of the used Geoeye-1 imagery.....	52
Appendix B- Error matrix of each scene.....	55

# List of figures and tables

## Figures

Figure 1.1) bathymetry of the Adriatic sea with emphasis on Losinj Island adopted from [http://en.wikipedia.org/wiki/Adriatic\\_Sea](http://en.wikipedia.org/wiki/Adriatic_Sea)

Figure 1.2) Satellite image of Losinj island, croatia adopted from bing maps

Figure 1.3) Geoeye-1 satellite in space

Figure 1.4) General methodological approach for the analysis of satellite images

Figure 2.1) Illustration of possible pathways of light in the atmosphere and water body. This figure is adapted from Robinson, 2004.

Figure 2.2) illustration of the linear relationship between DN and radiance

Figure 2.3) Diagram showing the probable change of the spectral signature in for different regions of the EM. The figure shows both the difficulty in discriminating different habitats by increasing depth and different spectral signatures for the same habitat in different depths. The picture is adopted from (Green et al., 2000).

Figure 2.4) Illustration of Lyzenga's method for water column correction. Notice that in step 3, depth would decrease from left to right. The picture is adopted from (Green et al., 2000).

Figure 3.1) Scene 0000001 before (A) and after atmospheric correction with FLAASH (B)

Figure 3.2) Scene 0000001 before (A) and after (B) atmospheric correction using ATCOR module

Figure 3.3) raster threshold mask converted to shapefile (A), and then manually edited to remove isolated water pixels that incorrectly categorized as land (B) and the final result after applying union, eliminate and dissolve operations orderly (C).

Figure 3.4) subset of land mass and boats from image 0000001

Figure 3.5) final result of masking land and boat areas.

Figure 3.6) linear regression of the glint samples between different band pairs

Figure 3.7) Scene 0000001 after glint correction.

Figure 3.8) Scene 0000001 after water column correction.

Figure 3.9) Scene 0000001 RGB: PCA1, Green, Blue

Figure 3.10) Chosen training points to train the supervised classifier

Figure 3.11) Maximum likelihood classifier results for scene 0000001

Figure 3.12) Maximum likelihood classifier results for scene 0010001

Figure 3.13) Maximum likelihood classifier results for scene 0010002

Figure 3.14) Maximum likelihood classifier results for scene 0020001

Figure 3.15) Mosaic of the edited classification result to cover whole Losinj Island

Figure 4.1) Plot of signature separability for merged training signatures for different bands (Band 1: Blue, Band 2: Green, Band 3: Red, Band 4: PCA-1) used in ML classifier.

## Tables:

Table 1.1) Geoeye-1 Satellite platform technical Information.

Table 2.2) Geoeye-1 satellite sensor characteristics.

Table 3.1) Gain and bias coefficients for Geoeye-1 satellite imagery

Table 3.2) input parameters of FLAASH module for all the scenes

Table 3.3) input parameters of ATCOR 2 module for all the scenes



Table 3.4) Area coverage of each bottom type

Table 4.1) Classification accuracy assessment report: Derived measures from Error Matrix for all scenes

Table 4.2) Average separability among the cluster center of class pairs in the merged training sample signature

## Abbreviations

ASCII (American Standard Code for Information Interchange)

ATCOR (ATmospheric CORrection)

BIL (Band Interleaved by Line)

BIP (Band Interleaved by Pixel)

DEM (digital elevation model)

DN (Digital Number)

DOS (Dark Object Subtraction)

ENVI (ENvironment for Visualizing Images)

EM (Electro-Magnetic Spectrum)

ESRI (Environmental Systems Research Institute)

FLAASH (Fast Line-of-sight Atmospheric Analysis of Spectral Hypercubes)

FUTBOLIN (FULL Transfer By Optimized LINE-by-line)

GeoTIFF (Geographic Tagged Image File Format)

GPS (Global Positioning System)

GRID (Global Resource Information Database)

IR (infrared)

ISODATA (Iterative Self-Organizing DATA Analysis Technique)

JPEG (Joint Photographic Experts Group)

LAI (Leaf Area Index)

ML (Maximum Likelihood)

MODIS (Moderate Resolution Imaging Spectroradiometer)

MODTRAN (MODerate resolution atmospheric TRANsmission)

MPA (Marine protected area)

NASA (National Aeronautics and Space Administration)

NIR (Near Infrared)

PCA (Principle Component Analysis)

RTM (Radiative Transfer Model)

SAV (Submerged Aquatic Vegetation)

TM (Thematic Mapper)

TOA (Top Of Atmosphere)

UNESCO (United Nations Educational, Scientific and Cultural Organization)

UTM (Universal Transfer Mercator)

WGS84 (World Global reference System)



# **Chapter 1: Introduction**

## ***1.1 General background on seagrass***

Seagrasses are submerged aquatic flowering plants rooted primarily in soft types of sediment (sand and mud) in coastal, estuarine and freshwater habitats all over the world (*Dennison et al., 1993; West, 1983*). Seagrasses are the only flowering plants which are adapted to live under water (*Short et al., 2007*).

Seagrasses are generally distributed alongside of tropical and temperate climate zones in near shore shallow waters between 0-50 meters depth (*McKenzie et al., 2003*). There are about 58 species of seagrasses worldwide which are divided to two orders (Hydrocharitales and Najadales), four families (Hydrocharitaceae, posidoniaceae, Cymodoceaceae and Zosteraceae) and twelve genera including *Enhalus*, *Thalassia*, *Halophila*, *Posidonia*, *Syringodium*, *Halodule*, *Cymodocea*, *Amphibolis*, *Thalassodendron*, *Zostera*, *Heterozostera* and *Phyllospandix* (*polina, 2011; Kuo et al., 1989*).

Besides the climate factors, seagrass distribution and growth is affected by other environmental factors such as chemical substances in the water, the accessibility to nutrients and turbidity of waves. Moreover, sedimentation rates and geological characteristics of the seafloor influence on seagrasses distribution (*McKenzie, 2003*).

*Zostera marina*, *Zostera noltii*, *Cymodocea nodosa* and *P.oceanica* are four main European seagrass species found in the Mediterranean Sea (*Polina, 2011*). However, *Posidonia Oceanica* is the dominant seagrass in the Mediterranean Sea, where it covers about 2% (about 50000 km<sup>2</sup>) of the seafloor on sandy and occasionally rocky beds (*Fornes et al., 2006; Larkum et al., 2006*).

## ***1.2 The importance of seagrass***

The vital importance of seagrass communities which makes them a key factor of coastal ecosystems is widely recognized (*West, 1983; Polina, 2011*). Seagrasses are an important component of the marine ecosystem food chain by their high rates of primary production (*Hossain, 2005; Pergent-Martini, 2005*). Furthermore, they serve as near-shore protection and nurseries for much juvenile marine life (*Wabnitz et al., 2008*) and their ability to store up to 12% of the total oceanic carbon makes them an important carbon sink for the ocean (*Bostrom, 2011*).

Also, seagrasses by acting as a barrier against currents and waves provide a natural protection against coastal erosion and also by trapping sediments; they keep the water clean and improve the quality of water (*Larkum et al., 2006*). Seagrasses are considered as a reliable indicator and

signifier of the environmental health of marine ecosystems and appropriate for the environmental monitoring (Polina, 2011; Fornes et al., 2006).

### **1.3 Seagrass threats**

Seagrasses are vulnerable to changes in coastal environments and can be easily destroyed or damaged. If the degradation is faster than the seagrass adaptation rate, then the result would be a reduction in the plants distribution area (Polina, 2011).

Threats can be due to natural and anthropogenic causes. Infectious diseases, competition among species, big storms such as hurricanes and tropical storms that produce both strong waves and high levels of turbidity which can destroy seagrass beds, are among the natural causes. But in comparison to nature, anthropogenic causes play the most important role in seagrass ecosystem degradation (Larkum and West 1990).

Direct human activities that threaten seagrass habitat include trawling and anchoring, seabed mining and dragging for oil, gas or mineral exploration and production, reduction in water clarity and quality because of dredge spoil, sewage sludge, industrial chemical waste, agricultural run-off and coastal development, anthropogenic noise of commercial and recreational boating (Seruci, 2010; Hossain, 2005; polina, 2011). Also indirect stress drivers such as acidification of the oceans, changes in ocean circulation, global sea level rise can be considered as the indirect role of humans in worldwide seagrass reduction due to increase in the concentration of greenhouse gases which lead to global warming (Harris, 2011).

In response to these challenging threats, policy makers and resource managers are trying to prevent, slow or reverse these negative changes by developing strategies introducing marine protected areas (MPAs) as a management tool (Aaby, 2004). Understanding the seagrass spatial distribution and characterization to create an accurate and up-to-date habitat map is a crucial step to the assessment of the ecosystem resource status and functions to reach the sustainable coastal zone management (Meyer, 2008).

### **1.4 Research problem: A remote sensing perspective**

Traditional methods of mapping seagrass are based mostly on in situ surveys or digitizing the seagrass extent from aerial photography which are both time consuming and labor intensive. Besides this, the spatial extend of seagrass meadows are highly variable and dynamic which makes delineating a hard boundary of their habitat an even more difficult task (Curran, 2011).

Due to its big scale view which is required to map an extensive area in a cost effective manner, many scientists consider remote sensing techniques as the most feasible mean to capture reference data for the purpose of map production at a suitable spatial resolution (Pulliza, 2004). Additionally

repetitive imagery from satellite sensors allow for routine monitoring of the selected areas and provide a cheap and accurate tool for performing a change detection analysis of the habitat.

Variations in seafloor coverage from seagrass to sand and rock can change the ocean color, expressed at the sea surface. These spectral contrasts can be used in an identification algorithm to group related spectral patterns into clusters and labeling them will produce a thematic map showing the seafloor cover types (*Arledge and Hatcher, 2008*). But marine remote sensing is very different from terrestrial applications and in many cases imposes challenges for benthic habitat mapping and requires special techniques to deal with water surface effects, water column attenuation and depth variation effects. For instance, IR bands which are commonly used in vegetation studies on land are not useful for mapping seagrass because they rapidly get absorbed by water column. Marine researchers can just rely on visible bands which can penetrate the water column to differentiate seagrass spectral reflectance from its surrounding covers. It means that the sensor is just restricted to shallow coastal waters at depths that visible light can penetrate but even in the shallow waters the turbidity in the water column and sun glint on the water surface can make the mapping process complicated and in some cases even impossible.

## **1.5 Research Objectives**

This study aims to explore the spatial distribution of *P.oceanica* seagrass along the coastline of Losinj Island based on remote sensing and GIS techniques. This research tries to evaluate the feasibility of employing semi-automatic image processing techniques to satisfy the increasing need of periodical seagrass maps in Croatia. Results of this study are expected to provide adequate information on both the pre-processing and classification methods which are appropriate to produce an accurate quantitative benthic map of seagrass habitats.

### **1.5.1 Specific objective**

To apply Geoeye-1 two meter multispectral satellite imagery for monitoring the distribution of *P.oceanica*.

### **1.5.2 Research question**

Does broadband Geoeye-1 imagery provide enough spectral and radiometric information to accurately distinct *P.oceanica* seagrass from sand and rocky beds, and therefore can be used for mapping of *P.oceanica*.

## **1.6 Study area**

The Adriatic Sea is the northernmost arm of the Mediterranean Sea, separating the Italian Peninsula from the Balkan Peninsula. The Adriatic contains over 1,300 islands, mostly located along its eastern, Croatian, coast with 1,246 counted (Leder et al., 2004). The sea is geographically

divided into the Northern Adriatic, Central (or Middle) Adriatic, and Southern Adriatic (Lipej et al., 2004).

Export of inorganic nutrients and import of organic carbon and nitrogen through the Strait of Otranto makes Adriatic a unique water body that gives rise to a rich flora and fauna (Bianchi, 2007).

Because of the counterclockwise direction of currents in the Adriatic Sea, it's eastern coast has relatively clearer and less polluted water than the western Adriatic coast. This circulation has significantly contributed to the biodiversity of the countries along the eastern Adriatic coast (Chemonics International Inc, 2000).

The North Adriatic basin, extending between Venice and Trieste towards a line connecting Ancona and Zadar, is only 15 meters deep at its northwestern end; it gradually deepens towards the southeast. It is the largest Mediterranean shelf and is simultaneously a dilution basin and a site of bottom water formation (Cushman-Roisin, 2002).

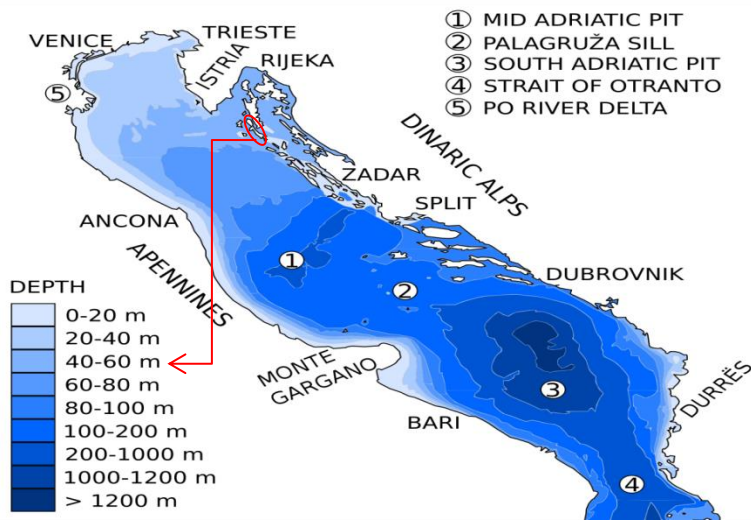


Figure 1.1) bathymetry of the Adriatic sea with emphasis on Lošinj Island adopted from [http://en.wikipedia.org/wiki/Adriatic\\_Sea](http://en.wikipedia.org/wiki/Adriatic_Sea)

Lošinj is a Croatian island in the northern Adriatic Sea, in the Kvarner Gulf (44° 35' 0" N, 14° 24' 0" E). It is almost due south of the city of Rijeka and part of the Primorje-Gorski Kotar County. The Island of Lošinj is part of the Cres-Lošinj island group that forms the most inland point of the Mediterranean Sea.

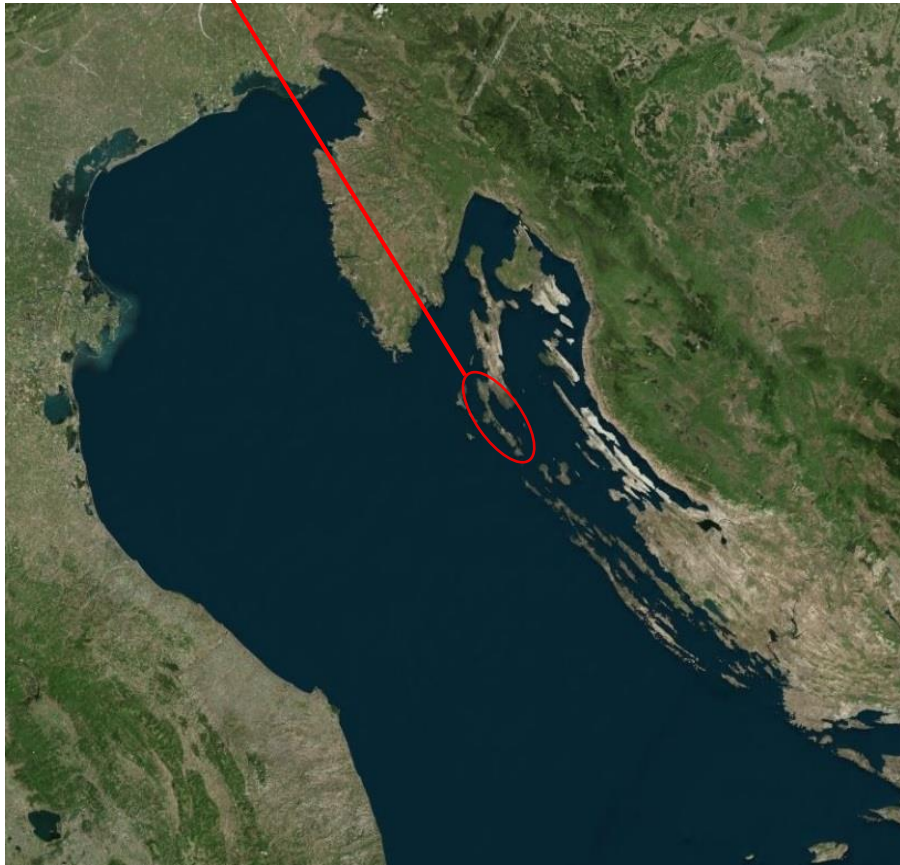


Figure 1.2) Satellite image of Losinj Island, Croatia adopted from Bing maps

Lošinj is the 11th largest Adriatic island by area (75 km<sup>2</sup>), 33 km long, with the width varying from 4.75 km in the north and middle of the island, to 0.25 km near the town of Mali Lošinj. The total coastline of the island is 112.7 km.

The island is formed predominantly of chalk limestone and dolomite rocks. It has a mild climate and evergreen vegetation (like myrtle, holm oak, and laurel). The highest elevations in the north have more sparse vegetation. Veli Lošinj, Čikat and the south-western coast are ringed by pine forests.

In the waters around the island of Losinj, there are 95 fish species, which is nearly a quarter of the total fish species found in the Adriatic Sea. Some of them have been severely depleted, particularly species such as the dusky grouper (*Epinephelus guaza*). Throughout the entire area there are large meadows of sea grass (*Posidonia oceanica*) known to be important for fish spawning, which have not yet been mapped. The area around Ćutin Veli and Ćutin Mali is dominated by coral communities characterized by different types of algae, corals and sponges. These coral communities live only in areas of high water purity with a small suspension of solid particles, many rare species are found here, some of which are protected, in particular the *Paramuricea chamaelon* and the red coral *Corallium rubrum*.

## **1.7 data sources**

### **1.7.1 Geoeeye-1 satellite imagery**

After IKONOS which was the first sub-meter commercial satellite, on September 6 2008, Geoeeye-1 was launched by Digital globe Company from Vandenberg Air Force Base, California with takes panchromatic images of 0.41 m and multispectral images of 1.65 m spatial resolution in RGB and NIR from a 684 Km orbital altitude in 15.2 Km swaths.

With its very high spatial resolution, accuracy and enhanced stereo for DEM generation and capacity to collect up to 700000 square kilometers of panchromatic imagery, Geoeeye-1 is believed as one of the most sophisticated commercial imaging satellites launched till now.

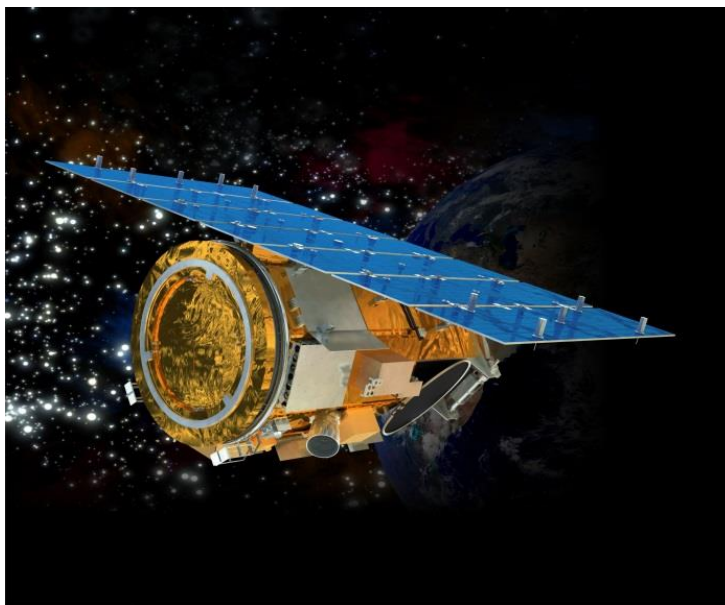


Figure 1.3) Geoeeye-1 satellite in space

Tables 1 and 2 provide an overview of Geoeeye-1 characteristics.



Table 1.1) Geoeye-1 Satellite platform technical Information

Name of satellite	GeoEye-1
Operating country	United States
Operating organization	DigitalGlobe, Inc.
Launch Date	September 6, 2008 (11:50:57 to 11:52:21 AM PST)
Satellite manufacturer	General Dynamics Advanced Information Systems (United States)
Launch Vehicle	Delta II
Launch Vehicle Manufacturer	Boeing Corporation
Launch Location	Vandenberg Air Force Base, California
Satellite Weight	1955 kg/ 4310 lbs
Satellite Storage and Downlink	1 Terabit recorder; X-band downlink (at 740 mb/sec or 150 mb/sec)
Orbital Altitude	684 kilometers / 425 miles
Orbital Velocity	About 7.5 km/sec or 17,000 mi/hr
Satellite orbit type/period	Polar sun-synchronous orbit/ 98 minutes
Orbital inclination	98 degrees
Equator Crossing Time	10:30 am
Operational Life	Fully redundant 7+ year design life; fuel for 15 years

Table 2.2) Geoeye-1 satellite sensor characteristics

<b>Imaging mode</b>	<b>panchromatic</b>	<b>Multispectral</b>
Spatial Resolution	.41 meter GSD at Nadir	1.65 meter GSD at Nadir
Spectral Range	450-900 nm	450-520 nm (blue) 520-600 nm (green) 625-695 nm (red) 760-900 nm (near IR)
Swath Width	Nominal swath width – 15.2 km at Nadir Single-point scene : 225 sq. km (15×15 km) Contiguous large area : 15,000 sq. km (300×50 km) Contiguous 1° cell size areas : 10,000 sq. km(100×100 km) Contiguous stereo area : 6,270 sq. km (224×28 km)	
Metric Accuracy/Geolocation	CE stereo: 2 m LE stereo: 3 m CE mono: 3.5 m These are specified as 90% CE (circular error) for the horizontal and 90% LE (linear error) for the vertical with no ground control points (GCP's)	
Off-Nadir Imaging	Up to 60 degrees	
Dynamic Range	8 bits/pixel , 11 bits/pixel	
Imaging Direction	Capable of imaging in any direction	
Daily Area Collection Capacity	Up to 700,000 sq. km/day of pan area Up to 350,000 sq. km/day of pan-sharpened multispectral area	
Revisit Time	Less than 3 day	
File formats	GeoTIFF (standard), NITF 2.0, NITF 2.1, JPEG, IMG	
Coordinate system	UTM (WGS84), Geographic (nominal ARC), Albers Conic Equal Area (ACEA), Lambert Conformal Conic (LCC), Transverse Mercator (TM) and State Plane projection (US only)	

## **1.7.2 Field work**

Field work was conducted by teaching institute of public health from Rijeka University in the period between 16<sup>th</sup> of May to 20<sup>th</sup> of May 2012. 400 point data were collected by scuba diving or using a Calfat viewer based on random stratified sampling design in order to both train the classifier and check the accuracy of the classification result. 180 points were used as training areas and the rest were used to measure the accuracy of the classification.

Samples were taken by a Garmin Oregon 450 GPS V with a positional accuracy between 3 and 5 meters. A depth for each point was collected with a GPS plotter/fish finder Garmin Echomap 50. Three main bottom types were selected after studying the area for image classification; seagrass communities (*P.oceanica*), mobile sediments (silt and sand ) and communities of hard substrate (rocks). Besides, shallow waters and deep waters were considered for classification. Unfortunately due to the lack of time and utility, the percentage of seagrass cover was not considered in the field visit.

## **1.8 software**

### **1.8.1 ENVI**

ENVI is an image processing package produced by ITT Corporation for the purpose of processing multispectral and hyperspectral remote sensing data (ITT, 2007).

ENVI 5 was used in this thesis as complement software besides ERDAS IMAGINE to perform atmospheric correction, glint removal and water column correction.

### **1.8.2 ERDAS IMAGINE**

ERDAS IMAGINE is developed by Intergraph which is one of the oldest and leading companies in geospatial world. The software package contains sophisticated tools for digital analysis of remotely sensed data.

Most of the image processing tasks in this thesis were done with the Imagine 2011 package.

## **1.9 Organization of the research**

This thesis seeks to contribute the use of remote sensing techniques to investigate the spatial distribution of *P.oceanica* as the dominant seagrass species in near-shore coastline of Losinj Island in Croatia.

Though chapter one covers the general background on seagrass, its importance and stress factors causing its decline, then explores the study area and the previous studies done on the subject. It then after giving the characteristics of the used satellite imagery in this thesis, it goes through a very brief explanation of the challenges and difficulties, researchers might encounter trying to produce an accurate benthic map.

Second chapter tries to widen our knowledge of the required algorithms to make the habitat map by going deeper into the concepts of each algorithm.

And at last in chapter three goes through the implementation of the algorithms and shows the results which will be followed by a discussion and a short conclusion at the end of the chapter.

Due to some problems with image quality which will be discussed in the third chapter, forced us to use an alternative methodology to produce the final thematic layer representing seafloor cover types. Diagram below is a general illustration of these two different methods.

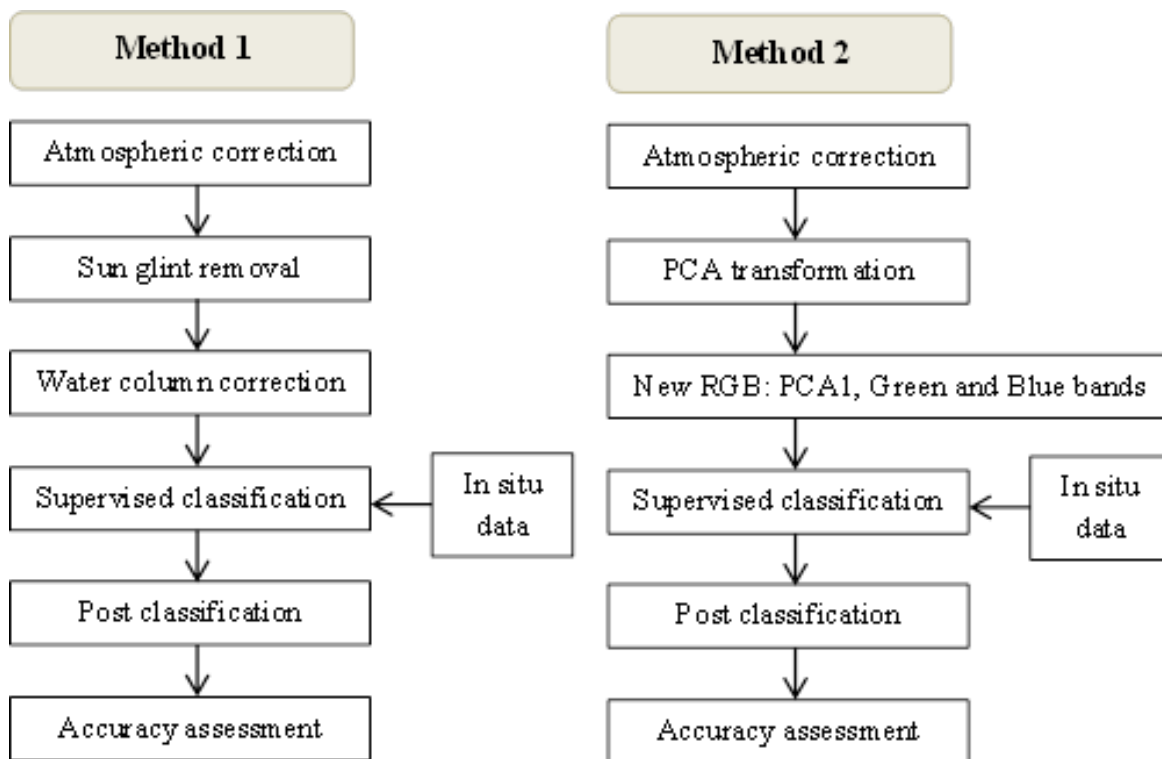


Figure 1.4) General methodological approach for the analysis of satellite images

## Chapter 2 – Theoretic background of the methods

### 2.1 Interaction of light with water body and atmosphere

In the last two decades satellite remote sensing at visible and NIR wavelengths became a powerful tool in studying marine ecology and its conservation. Medium resolution sensors like MODIS and MERIS were routinely used to estimate the concentration of chlorophyll and monitor phytoplankton activities which improved our understanding of the oceanic productivity. Also with the help of high resolution imageries (e.g IKONOS, QuickBird), mapping the benthic habitats even at the species level become possible. However, it should be considered that the reflectance which reaches the sensor on the satellite platform has both interacted with water column and travelled through the atmosphere.

Absorption and scattering are main processes when electromagnetic radiation passes through the atmosphere and water mediums. Actually the majority of the signal received by the sensor is due to atmospheric and water column scattering and only about the 10% of the received signal comes from the sea bottom (Robinson, 2010). So the sea and air interactions must be taken into account when satellite imagery is being used in marine environmental studies such as benthic habitat mapping.

Figure (2.1) shows the complexity of interactions between solar radiance and atmosphere and sea which are important in marine remote sensing.

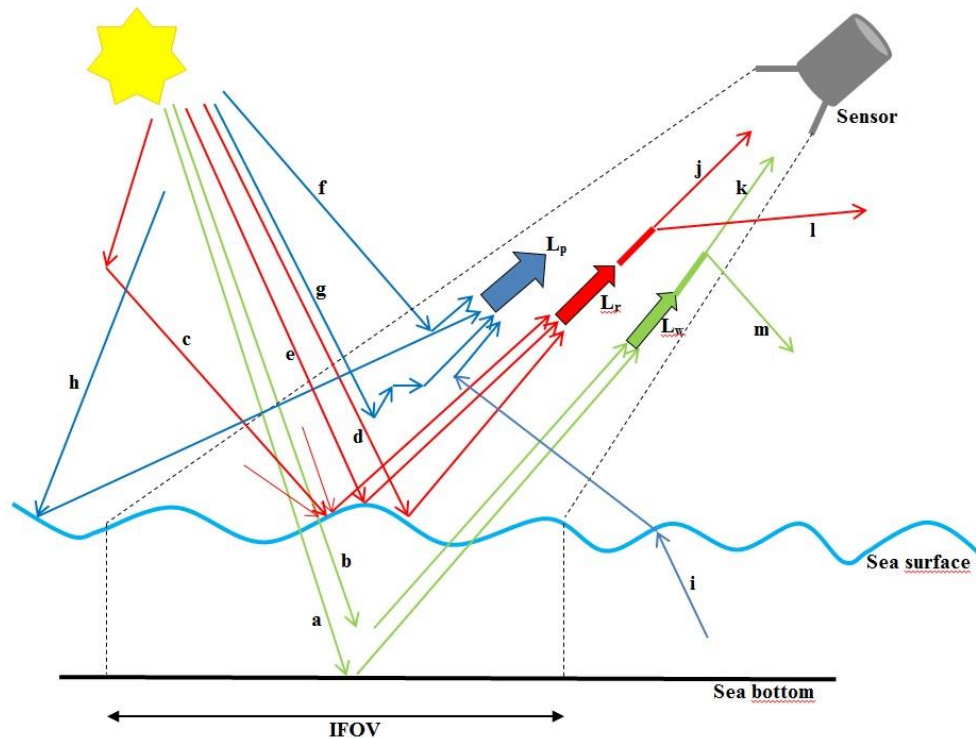


Figure 2.1) illustration of possible pathways of light in the atmosphere and water body. This figure is modified from Robinson, 2010.

Equation 1 (Robinson, 2010) shows the total radiance ( $L_t$ ) that reaches the sensor which can be defined as:

$$L_t = L_p + TL_r + TL_w \quad (1)$$

Where

$L_p$  is the total path radiance

$L_r$  is the total water surface reflection

$L_w$  is the water leaving radiance

And T is the beam transmittance of the atmosphere.

Based on figure (2.1) each of the contributing parameters of equation (1) can further be divided to smaller parts.

$$L_p = f + g + h + i, L_r = c + d + e, L_w = a + b \quad (2)$$

**a:** is the bottom radiance which has the most important portion of detector's receiving radiance for benthic classification and mapping.

**b:** is the subsurface radiance. This is the portion of  $L_w$  which gets scattered in the water column and emerged to the sensor without reaching to the sea bottom.

**c:** is the sky glint. This is the scattered light from the atmosphere that reaches the sea surface and gets reflected to the sensor.

**d:** is sun glint. This is the specular reflection of sunlight from the surface of the sea. A detailed explanation of sun glint and its correction methods is given in this chapter.

**e:** is representing the reflection from white caps on the sea surface. It's worth mentioning that correction of whitecap reflection needs additional data like the wind speed and direction, temperature of the near surface water and air temperature in hourly basis as an input for sophisticated algorithms to model the wave patterns (Callaghan et al., 2008).

**f:** is part of the path radiance that the sunlight directly scattered toward the detector.

**g:** is the part of path radiance that the sunlight get directed toward the sensor after several scattering in the atmosphere.

**h:** is the surface reflectance which is from the outside of the sensor's field of view but get directed toward the sensor because of atmospheric scattering.

$i$ : is the reflection from water body which does not belong to the sensor's field of view but get scattered to the sensors field of view.

Also we should notice that due to the atmospheric scattering (terms  $\mathbf{l}$ ,  $\mathbf{m}$ ) even  $L_r$  and  $L_w$  will attenuate (terms  $\mathbf{j}$  and  $\mathbf{k}$  respectively) before they get recorded by the sensor's detectors.

Equation (1) clearly shows the big contribution of atmospheric path radiance and water surface reflection in the receiving radiance by the sensor and the necessity of removing them for benthic habitat studies.

## **2.2 Atmospheric correction**

Satellite imagery is largely affected by the absorption and scattering caused by atmospheric gases and particles. So the objective of atmospheric correction is to retrieve the surface reflectance by removing (or at least greatly reducing) the atmospheric effects from the top of the atmosphere radiance which will improve the accuracy of image classification and is a necessary step in many multi-temporal, multi-sensor and quantitative analyses (Lillesand and Kiefer, 2007).

Atmospheric correction methods can be categorized into three groups:

1. Radiance to reflectance conversion
2. Relative atmospheric correction methods
3. Absolute atmospheric correction methods

### **2.2.1 Radiance to reflectance conversion**

Each pixel in satellite imagery has an integer value assigned to them which is known as digital number (DN). Although DNs provide a convenient display and simplify the computation, they do not represent the earth surface brightness in physical units (watts per square meter per micrometer per steradian) which is necessary for many physical processing models in environmental studies (Campbell and Wynne, 2011). The good news is there is a linear relationship between DN values and radiance (figure 2.2). So by knowing the sensor's calibration factors, DNs can be easily converted to radiance using equation 3 based on the Geoeye-1 technical report or following equations (4 to 6) by Markham and Barker (1986).

$$DN = Gain * spectral\ radiance\ (L) + offset \quad (3)$$

$$L = \left( \frac{L_{max} - L_{min}}{DN_{max}} \right) DN + L_{min} \quad (4)$$

Where

$L_{min}$  and  $L_{max}$  are respectively the minimum and maximum spectral radiance at the range of rescaled radiance. Rescaled radiance range is referred to the radiometric resolution of the sensor. For example for an 8-bit image, rescaled radiance range of  $L_{min}$  would be zero and for  $L_{max}$  it is equal to 255.

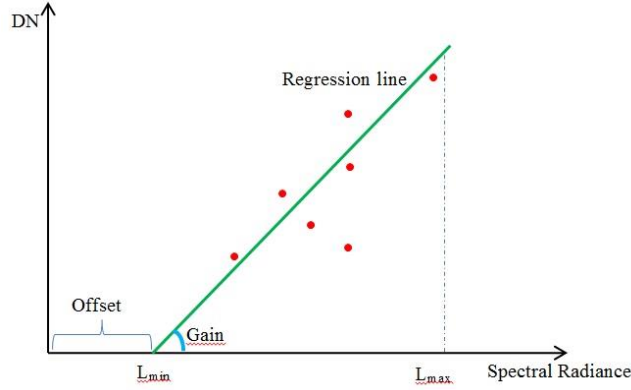


Figure 2.2) illustration of the linear relationship between DN and radiance

Reflectance is defined as the relative brightness value of an earth surface object measured for a specific wavelength interval. To calculate reflectance we need to estimate the incident radiance upon the object at the time of image acquisition. Precise measurements need in situ data and a proper knowledge of the atmospheric condition which are not available most of the time (Campbell and Wynne, 2011). Equation (5) without going through the precise measurement gives us a good estimation of the top of the atmosphere reflectance.

$$\rho = \frac{\pi L d^2}{E_{SUN} \cos(\theta)} \quad (5)$$

Where

$\rho$ : is the top of the atmosphere reflectance. Because reflectance is a ratio, it is unitless and can vary between 0-1.

$L$ : is the spectral reflectance which is the result of equation (3) or (4).

$d$ : is the earth-sun distance is astronomical unit and can be calculated based on the Julian day of the image acquisition from the equation below.

$$d = 1 - 0.01672 * \cos[0.9856(Julian Day - 4)] \quad (6)$$

$E_{SUN}$ : is the exoatmospheric spectral irradiance which is specific for each sensor and each band. This value is provided for the sensor manufacturer.

$\theta$ : is the sun zenith angle in degree which is usually available in image metadata.

Conversion of radiance to top of the atmosphere (TOA) reflectance will remove the effects of sun elevation angle, different values of the exoatmospheric solar irradiance arising from spectral band differences and differences of earth-sun distance at the time of image acquisition (Chander et al., 2009). This will make the multi-temporal and multi-sensor analyzes possible but it will not remove the path radiance (Lillesand et al., 2007).

### **2.2.2 Relative atmospheric correction methods**

Relative atmospheric methods do not evaluate any kind of atmospheric components, instead by applying empirical (statistical) models they try to provide a good estimation of the surface reflectance. These statistical models are fast, easy to implement and they usually rely on the image itself without a need for additional information. Here we try to briefly go through some of the most popular empirical models among remote sensing researchers.

Due to its simplicity, the Minimum Histogram method (also called Dark Pixel Subtraction) is one of the most popular relative corrections among remote sensing scientists. This method is based on the fact that the reflectance of a very dark target like deep water in infra-red interval of EM or dark shadow should be zero or very close to it. So any recorded radiance in those pixels is the result of atmospheric path radiance. To perform the atmospheric correction, the minimum value of this residual radiance would be subtracted from all the pixels in that band. There are more sophisticated varieties of dark pixel subtraction method which combine the dark target radiance with atmospheric modelling but with no complex atmospheric measurements (Schowengerdt, 2007). For further information see (Chavez, 1989) and (Tanre et al., 1990).

Another easy to implement technique is the regression method, like DOS (Dark Object Subtraction), in this method some samples will be taken from dark pixels both in the infra-red and visible bands. Then the spectral values from the two bands would be plotted against each other (infra-red band on the Y and the visible band on the X axis). Then, a first order polynomial will be fitted to the points using linear regression and the bias on the X axis would be considered as the path radiance for that visible band and will be subtracted from all pixels (Kokko, 2008).

Both DOS and regression method are relying on the image itself to remove the path radiance. And they both need the presence of a dark object to do so. Also these models assume that the surface is lambertian and the effect of the atmosphere is constant through the whole image which might not be the case most of the time.

Another relative atmospheric correction can be made using the empirical line method. In this method two targets would be chosen on the image one dark object and one bright one. The reflectance of these two objects will be measured on the ground and would be plotted against the spectral radiance value of the same targets on the image. The slope of the line will be considered as the atmospheric radiance and the interception would be the path radiance (Kawishwar, 2007).

### **2.2.3 Absolute atmospheric correction methods**

Absolute atmospheric correction methods take advantage of using radiative transfer models to simulate the process of transferring an EM wave in the atmosphere. The needed parameters to make an atmospheric profile can be gathered with in situ measurements at the time of image acquisition or can be indirectly based on the image header data. Due to lack of accurate measured atmospheric data, radiative transfer codes were developed to work with atmospheric profiles but it might cause an un-estimated error in the resultant ground reflectance (Kawishwar, 2007).



Since 1972, a great effort was done to develop reliable radiative transfer codes for the purpose of making atmospheric correction models for satellite imagery. Now, there are many radiative transfer models (RTMs) available such as 5S, 6S/6SV1, MODTRAN, XRTM, FUTBOLIN.

MODerate spectral resolution atmospheric TRANsmittance algorithm (MODTRAN) is the most popular and commonly used radiative transfer code which is developed by US Air Force research laboratory. MODTRAN calculates atmospheric transmittance and radiance for frequencies ranged from 0 to 200 nm at moderate spectral resolution of 0.0001  $\mu\text{m}$  (Kneizys et al., 1996).

Atmospheric CORrection Now (ATCOR), Fast Line-of-Sight Atmospheric Analysis of Spectral Hypercubes (FLAASH) are the two commonly used atmospheric models based on MODTRAN 4 to calculate the atmospheric look-up tables. These models are available as ready-made module in ERDAS IMAGINE and ENVI software suits respectively and been used in this thesis to perform the atmospheric correction.

### ***2.3 Sun glint correction***

The surface of open sea is almost always affected by the blowing wind which generate waves with the magnitude that is strongly related to the strength of the wind (NASA, 2003). The presence of these waves will disperse the reflected solar radiance from the water surface and cause a phenomenon called sun glint.

In technical literature, sun glint is defined as the specular reflection of sunlight directly from a non-flat water surface (wind driven waves) toward the sensor and is dependent on the state of water surface, position of sun and viewing angle of the sensor (Hochberg et al., 2003).

Unfortunately the effect of sun glint is most obvious in clear, shallow waters when the image has a very high spatial resolution and the cloud coverage is minimal (Wicaksono, 2012).

A big portion of the radiance that reaches the sensor is due to sun glint which makes both the visual interpretation and classification of the benthic habitats a very difficult task (Deidda and Sanna, 2012). So developing a robust algorithm to remove the effect of glint is a necessity.

Sun glint correction techniques can be widely categorized in two big groups based on the spatial resolution of the imaging sensor. There are many methods (Wang and Bailey, 2001; Montanger et al., 2005; Fukushima et al., 2007; Ottaviani et al., 2008; Doerffer et al., 2008) developed to remove the glint in coarse resolution satellite imagery with the resolution of bigger than 100m which glint is estimated based on the probability distribution of sea surface slopes and depend on the wind speed and direction. But in high resolution images with the pixel size of less than 10 m, the pixel size is not much bigger than water surface features which make the statistical assumption of previous methods about a surface composed of many reflecting facets, invalid (Kay, 2011).

On the other hand, methods to remove sun glint from high resolution imagery (Hochberg et al., 2003; Hedley et al., 2005; Philpot, 2005; Goodman et al., 2008; Kutser et al., 2009) are based on using the NIR bands to estimate the amount of glint in the receiving signal and then subtract it.

Hedley's method is used in this study which is an update of Hochberg method. Beside a simpler implementation steps, Hedley's method is less sensitive to outlier pixels and it does not require the time consuming process of masking out cloud and land pixels prior the de-glinting process but both of the methods rely on the same two initial assumptions. (Hedley, 2005).

Because of the strong absorption of light in 700-1000 nm wavelengths by water molecules, even shallow water is relatively opaque to NIR wavelengths regardless of the bottom type (Mobley, 1994). This will lead us to the first assumption that the brightness values in the NIR band can be considered as an offset caused by sun glint and a spatially constant ambient in the case that the image is not atmospherically corrected (Hedley, 2005).

The second assumption is that there is a linear relationship between the amount of sun glint in visible bands and the brightness values of the NIR band (Hochberg et al. 2003). The equality of the real index of refraction (bending of light when passing through two media with different mass which are transmitting light) for both NIR and visible wavelengths is justifying this assumption (Mobley, 1994).

To implement the method, the linear relationship using an empirical model (linear regression) would be established between the visible and NIR bands to obtain the gradient of calibration (slope of the regression model) of different sun glint intensities occurred on both bands.

The slope then will be used as a coefficient in the following equation based on Hochberg et al. (2003) and Hedley et al. (2005) works to de-glint the pixels in the image.

$$R'_i = R_i - [b_i(R_{NIR} - Min_{NIR})] \quad (7)$$

Where

$R'_i$  is the brightness of sun glint corrected pixel in band i

$R_i$  is the uncorrected pixel value for band i

$b_i$  is the regression slope between visible band i and the NIR band

$R_{NIR}$  is the pixel value in the NIR band

$Min_{NIR}$  is the lowest NIR value in the image (ambient NIR level)

## **2.4 Water column correction**

One of the main difficulties of benthic mapping is the influence of variable depth on the reflectance of sea bed features (Mumby et al. 1998). It's because the intensity of the penetrated light into water will decrease exponentially with increasing depth. This process is called radiance attenuation in literature and it is wavelength dependent. Longer wavelengths like red and infra-red part of EM will attenuate more rapidly than shorter wavelengths like blue and green light (Green et al. 2000).

Therefore attenuation will cause two major effects. 1) By increasing depth, the spectral separability of the substrate features would decrease. 2) There would be spectral signature confusion while doing the multispectral classification of the habitats. For example the spectral signature of seagrass would be much different from 2 m to 20 m depth (big inter-class variance) or the signature of sand in 5 meter might be similar to seagrass in 15 meters.

Decreased intensity of light while passing through the water column is the result of absorption and scattering in the water which is caused by the presence of dissolved and organic matter in the water like suspended particulate matter and phytoplankton (Arce, 2005).

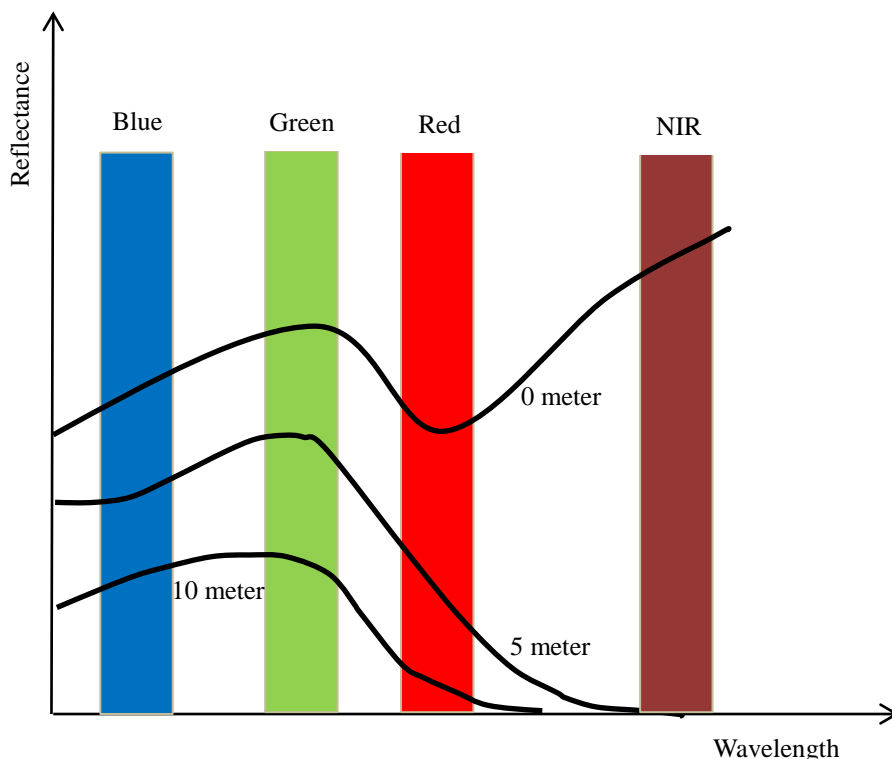


Figure 2.3) Diagram showing the probable change of the spectral signature in for different regions of the EM. The figure shows both the difficulty in discriminating different habitats by increasing depth and different spectral signatures for the same habitat in different depths. The picture is modified from (Green et al., 2000).

Having optical properties of water in mind Morel and Prieur (1977) classified natural water in two groups. Case I consist of phytoplankton dominated waters and in case II water is dominated by inorganic particles (Arledge R.K., Hatcher E.B., 2008). A more detailed classification system was developed by Jerlov (1976) based on water optical attenuation properties. This system divides oceanic water to three main categories. Type I represent the extremely clear water. Type II is the clear oceanic water with the attenuation greater than that of low productivity waters and type III consist of the most turbid waters which usually found in coastal areas (UNESCO 1999).

Removing the effect of depth on bottom reflectance would require both a depth value for each water pixel in the image with a measurement of the water column attenuation characteristics (Mumby et al. 1998). Due to the absence of bathymetric and water column properties data at the

time of imaging, Lyzenga's (1978, 1981) empirical technique was applied to decrease the attenuation effect of water column. Lyzenga's method tries to compensate the water column attenuation effects to produce a depth invariant index from each pair of spectral bands with an initial assumption that as long as the attenuation coefficients are the same in each pair of bands then the ratio of two distinct substrate cover would not be dependent to water depth (Pahlevan et al., 2006).

Also it's worth mentioning that almost all of the studies assumed that  $K_d$  (local light attenuation) values extracted from few samples from an area in the image can be used for other regions too but the attenuation coefficient might show high spatial variability especially in tropical areas (Karpouzli et al. , 2003).

The Lyzenga technique can be divided to several steps as follows (UNESCO 1999):

**1- Atmospheric and sun glint correction**

As discussed in the atmospheric correction part, prior to water column correction we should remove the path radiance caused by atmospheric scattering and the water surface reflectance (sun glint).

This can be done by using a radiative transfer model or a simple crude correction like dark pixel subtraction (DOS).

$$\text{Atmospherically corrected radiance} = L_i - L_{si} \quad (8)$$

Where  $L_i$  is the pixel radiance in band  $i$  and  $L_{si}$  is the average radiance of deep water for band  $i$ . Because we did the atmospheric correction before for the rest of the steps we consider  $L_i$  as the atmospherically corrected pixel radiance of band  $i$ .

**2- Make a linear relationship between radiance and depth**

Lyzenga's method is based on the assumption that the decrease in the light intensity with the increasing depth follows an exponential curve (Mumby et al., 1998). In this step by using the natural logarithm ( $\ln$ ), the relationship between depth and radiance becomes linear.

$$X_i = \ln(L_i) \quad (9)$$

**3- Calculate the ratio of attenuation coefficients for band pairs**

Attenuation coefficient shows the severity of the decrease of light intensity for each band through the water column and can be calculated with the following formula.

$$L_i = L_{si} + a.r.e^{(-2k_jz)} \quad (10)$$

In this formula  $r$  is the reflectance of bottom which we seek but the problem is we have many unknowns like the constant  $a$ ;  $k_j$  which represents the attenuation coefficient for band  $j$  and  $z$  which is the depth value for each pixel.

The beauty of the Lyzenga's method is by using the ratio of two bands it cancels out these unknown parameters and make the calculations just base on the image itself.

The ratio of the attenuation coefficient can be defined with the formula below.

$$\frac{K_i}{K_j} = a + \sqrt{(a^2 + 1)} \quad (11)$$

“a” is based on the variance and covariance of the band pairs i and j and can be calculated as follows.

$$a = \frac{\text{Var band } i - \text{Var band } j}{2 * \text{Cov bands } i \text{ and } j} = \frac{\sigma_{ii} - \sigma_{jj}}{2 \sigma_{ij}} \quad (12)$$

$$\sigma_{ij} = (\overline{X_i X_j}) - (\overline{X_i} * \overline{X_j}) \quad (13)$$

And X is the natural logarithm of pixel reflectance (L) for each band.

To implement this part, some pixel samples will be taken for a known substrate type in different depths from each band. Then a bi-plot would be made and the slope of the plot shows the ratio attenuation coefficient for that pair of bands.

#### 4- generate a depth-invariant index of bottom type

Because the samples belong to a unique bottom type and due to the linearization of the relationship between radiance and depth, pixel values shape around a line on the bi-plot. By adding the reflectance value of different bottom types on the bi-plot based on their reflectance they would make several almost parallel lines but the y-intercept would be the same for each substrate.

So the depth invariant index can be build based on the equation of a simple line.

$$y = b + ax \Rightarrow b = y - ax \quad (14)$$

$$\text{Depth invariant index} = \ln(L_i) - \left[ \left( \frac{K_i}{K_j} \right) * \ln(L_j) \right] \quad (15)$$

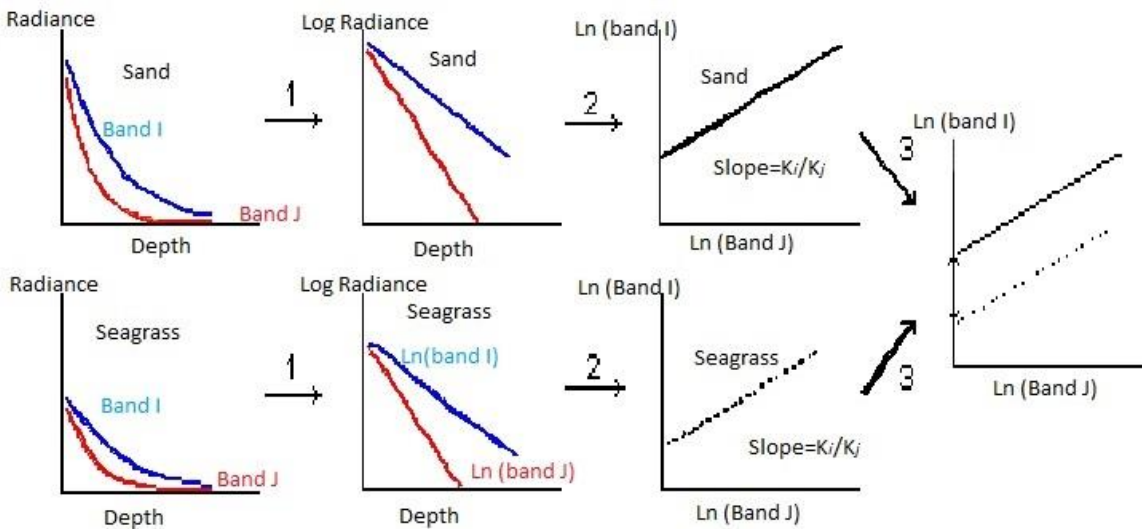


Figure 2.4) Illustration of Lyzenga's method for water column correction. Notice that in step 3, depth would decrease from left to right. The picture is adopted from (Green et al., 2000).

## 2.5 Principle Component Analysis (PCA)

Principle component analysis is a multi-variable statistical operation to transform the coordinates of the data in multidimensional feature space based on the correlation between bands (Das). In the field of digital processing of multi and hyper spectral satellite imagery, PCA can be used to reveal the most informative bands and by un-correlating the bands, it can reduce the dimensionality of the dataset and compress the image data. Also transforming the DN values and redistributing those onto new orthogonal axes might increase the spectral separability of some classes which their spectral signatures had partial overlap before the transformation (Gao, 2009).

Process of PCA can be divided into these steps (Tso and Mather, 2009).

1. Calculate the mean of all the pixel values in each band.
2. Subtract the mean value from all the pixel values in that band. This will produce a dataset with the mean of zero.
3. Calculate the variance-covariance (or correlation) matrix. The dimension of the covariance matrix should be equal to the number of image bands.
4. Compute the unit eigenvectors and related eigenvalues for the covariance matrix. If a  $n \times n$  covariance matrix does have any eigenvectors then the number would be equal to  $n$ .
5. Order the eigenvectors by eigenvalues from highest to lowest. Then make a feature vector by forming a new matrix from the eigenvectors we want to keep.
6. Rotating the feature space based on the selected eigenvectors in the feature vector.

The first principle component image which is derived from the first eigenvector with the highest eigenvalue would have the biggest amount of total variance in the dataset. Because in image processing variance usually relates to information, PCA1 would contain most of the useful information of all input bands. And the variance of the remaining PCA images would decrease in correspondence to decrease in magnitude of their eigenvalues (Tso and Mather, 2009).

PCA based on the variance-covariance matrix is called unstandardized PCA in the technical literature while the standardized PCA is based on the correlation matrix. If the images are in DN values or does not have the same unit then it's better to use the standardized PCA. Correlation can be calculated by subtracting the mean value from all the measurements and then divide the results by the standard deviation. This procedure will make each spectral band with a unit variance and a mean of zero, hence, normalize the data onto the same scale (Mather, 2011).

It should be noticed that if the image units are compatible like when the image is converted to radiance, then it's better to use unstandardized PCA because normalization in the correlation matrix will cost us changes in the degree of variability between the bands (Tso and Mather, 2009).

## **2.6 Classification**

Digital image classification is the process of converting a numerical image data into a thematic map. Classification is the an important step in remote sensing and digital image processing because in many instances, the resultant thematic map of this process is considered as the final product of the analysis but even in the cases that the classification result is an intermediate step in a more complex analysis, one cannot ignore the importance of its reliability in the total accuracy of that analysis.

A specific algorithm to perform the image classification is called classifier in the technical literature. There are a wide variety of these classifiers and each of them tries to use a classification procedure to improve the classification accuracy. Classifiers can be categorized into several groups based on different views.

They can be divided into soft and hard classification methods based on how the feature space decision boundary of the classifier is defined. The most common way is to categorize the classifiers into two general groups of supervised and unsupervised classification methods.

Unsupervised classifiers such as ISODATA and K-mean can be defined as finding of the natural spectral clusters within the multispectral data without having a prior knowledge in the case of representative ground samples to train the classifier but of course we need a general knowledge of the area covered by the image scene in order to interpret the results (Campbell, 2011).

On the other hand, supervised classification use samples with known information class to train the algorithm to classify pixels of unknown identity. Most popular supervised classifiers are minimum distance, parallelepiped and maximum likelihood.

Unfortunately selecting the best classification method is not an easy task. Many factors such as the source of the image data and its characteristics, chosen classification system, complexity of the landscape, quality of the training data and even software availability are among the major factors that affecting the choice of a proper classifier (Lu & Weng, 2007).

This work used Maximum likelihood classification method because among the above mentioned classifiers it's the only one that can consider the spectral variability within each class that might be because of atmospheric or mixed pixel effects by using the mean, variance and covariance of each

class from the training samples. This means that ML classifier is extrapolating the statistical parameters of each class from the training data. This extrapolation is based on two main assumptions. First, the training samples must be a good representative of classes and second, they should have a multivariate normal frequency (Gaussian) distribution. Violating these assumptions may reduce the accuracy of the classification (Campbell, 2011).

Maximum likelihood (ML) is a statistical supervised classifier which is based on Bayesian probability formula to calculate the probability of the belonging of a pixel to a set of pre-defined information classes. The pixels will be assigned to a class with the highest probability (Tso and Mather, 2009). This can be shown with equation 16.

$$X \in C_j \text{ if } p(C_j|X) = \max[p(C_1|X), p(C_2|X), \dots, p(C_m|X)] \quad (16)$$

In the above formula  $p(C_j|X)$  is the conditional probability of pixel X being a member of class  $C_j$  which can be solved using the Bayesian theory (Eq. 17).

$$p(C_j|X) = \frac{p(X|C_j) \times p(C_j)}{p(X)} = \frac{p(X|C_j) \times p(C_j)}{p(C_1) p(X|C_1) + p(C_2) p(X|C_2) + \dots + p(C_m) p(X|C_m)} \quad (17)$$

$p(X|C_j)$  is the probability of encountering of a specific DN value, given that we have category  $C_j$  which can be estimated from the training samples.

$p(C_j)$  denotes the probability of occurrence of a specific information class in the image but this is impossible to know this value before the classification. To solve this issue we have two options. We can assume that the probability is equal for all the information classes or derive the value from the results of previous classifications either supervised or unsupervised.

$p(X)$  is the probability of occurrence of a specific DN value in the image which is estimated by multiplying the probability of finding that DN in a class by the probability of that class and summing it up for all the available information classes in the imagery.

$$p(C_j|X) = \frac{p(X|C_j)}{\sum_{i=1}^m p(X|C_i)} \quad (18)$$

Equation 18 is the simplification of the Bayesian formula which shows that the calculations will reduce to estimating  $p(X|C_j)$  which is justifying the above mentioned assumptions about training data (Gao, 2009).

### 2.6.1 Post-classification

Complexity of the earth surface usually causes a spectral confusion among information classes which leads to isolated pixels in the classification result of the common supervised classifiers. This will make a salt-pepper effect on the resultant thematic map which can be reduced by using a mean or majority filter (Lu & Weng, 2007).



## **2.7 Accuracy assessment**

It's common knowledge among scientists of different fields that it is impossible to find a model which is the perfect representative of reality. The same rule applies to the maps generated from image classification procedure. So before we can use a map in an application, we should have an indication of its quality to see if it meets the requirements of that specific application.

Accuracy assessment is the procedure to determine the degree of error (incorrect labelling of pixels) in the resultant thematic map (Mather, 2011). The most common way to assess the classification accuracy can be achieved by using an error matrix which is also known by the name of confusion matrix in technical literature (Tso and Mather, 2009).

Confusion matrix is a square matrix with a dimension equal to the number of classes. The matrix represents the relationship between two sample sets, reference dataset which is collected by field work or using the existing maps with the pixel labels made by the classifier which is correspond to the reference data (Tso and Mather, 2009). The columns in the matrix are showing the reference data while the rows are representing the pixel labels assigned by the classifier (Mather, 2001).

Confusion matrix can be used to derive some statistical parameters to indicate the quality of the data. The simplest parameter is the overall accuracy which can be obtained by dividing the major diagonal (number of correctly classified pixels) of the matrix by the total number of pixels (total row or column sum) (Gao, 2009).

As it comes from the name, overall accuracy is just giving us a total view of the classes as a whole. For computing the accuracy of individual classes we need two other parameters, namely producer's and user's accuracies.

Producer's accuracy (omission error) shows us the probability how correctly a pixel of reference dataset can be recognized by the classifier. This parameter is measured by dividing the total number of correct pixels in a class by the total number of pixels in that class derived from reference data (column sum). On the other hand, user's accuracy (commission error) will show us how well the classified pixel on the image is representing the information class on the ground. This parameter can be calculated by dividing the total number of correct pixels in a class divided by the total number of the pixels in that class (sum of the row) (Congalton, 1991).

On the other hand Cohen's kappa coefficient gives a measure of agreement between the achieved model and reality by determining how significantly the result of the error matrix is better than pure chance (Jensen, 1996).

## **2.8 Previous works**

Various techniques have been developed to assess and monitor the spatial and temporal changes of seagrass habitat such as field survey methods consisting of permanent transect monitoring to different variations of random sampling design. Also aerial photography has been used extensively for developing habitat maps.

Seagrass biomass is very sensitive to environmental disturbance and the traditional surveying methods are mostly based on sampling small areas and extrapolating the results to a much larger area which might not be reliable enough for local and regional studies. On the other hand, satellite remote sensing is capable of providing a reliable and consistent database of the benthic habitat repeatedly over very large areas and in a cost effective and timely fashion.

Wabnitz et al. (2008) tried to use Landsat imagery to produce large scale baseline habitat maps of the Caribbean Sea. To achieve this goal, they used geomorphological segmentation, contextual editing and supervised classification. For accuracy assessment beside using in situ data, they took advantage of high resolution IKONOS imagery and previously published habitat maps with documented accuracies and reached the overall accuracies of 46 to 88% for about 40 Landsat 5 and 7 scenes which they concluded to be acceptable for regional baseline maps for large scale conservation programs.

Fornes et al. (2006) used supervised classification technique on multispectral IKONOS imagery to monitor *P. oceanica* in shallow coastal waters around Balearic Islands in western Mediterranean Sea. They used maximum likelihood decision rule to classify pixels into four classes: sand, rock, *P. oceanica* and unclassifiable pixels. Then they compared their result with a reference acoustic seabed classification and got 84% agreement for chosen sample areas.

Mumby et al. (1998) did water column correction and contextual editing followed by a supervised classification as part of their framework analysis to make benthic habitat maps on various sensors including CASI, Spot and TM images of Truks and Caicos islands (British West Indies) and concluded that doing water column correction will improve the accuracy of the classification's result by 13% in CASI, up to 6% in TM imagery but it is not significant for sensors which produce a single depth invariant band like SPOT-XS and Landsat MSS.

Sagawa et al. (2010) developed a new index for radiometric correction based on bathymetric data and attenuation coefficient to model the relationship between bottom reflectance through the water column and radiance level measured by satellite. They tested the model using two case studies: Funakoshi Bay in Japan and Gabes Gulf (Mahares), Tunisia representing Jerlov water types II and II to III respectively. After applying their new reflectance index on IKONOS imagery, they followed the analysis using a maximum likelihood supervised classification to generate a habitat map and got the overall accuracy of 83.3 and 90% respectively for Funakoshi Bay and Gabes Gulf which shows an improvement in the accuracy of the resultant benthic map in comparison to traditional depth invariant index based on Lyzenga's model.

Pu et al. (2012) used Landsat 5 TM, ALI and Hyperion satellite imagery, all with 30 meter spatial resolution, with regards to two metrics namely percent cover of submerged aquatic vegetation (SAV%) and leaf area index (LAI) for monitoring seagrass habitats within shallow coastal areas along the central coast of Florida, USA. They did the analysis first by converting the DN values to

at-water surface reflectance. Then calculated the depth invariant bands from calibrated reflectance for all the three sensors and continued with a supervised classification of SAV cover into two classification schemes, one with 3 and the other one with 5 classes. Then both metrics were measured in the field using a spectroradiometer and six multiple regression models were developed to compare the spectral variability of the metrics from different sensors. Regression models showed that Hyperion hyperspectral data produced the best seagrass maps in both of the classification schemes which is due to its better spectral and radiometric resolution, the results from ALI outperformed the maps from TM data in both classification schemes. Also they found that the water depth correction approach effectively improves the classification result of the seagrass habitats in all the three sensors.

## **Chapter 3 – Implementation and result**

### ***3.1 Image processing overview***

This chapter goes through the implementation of the processing methods, for a methodology to create a seagrass habitat map from Geoeye-1 multispectral satellite imagery and the result of each step is included. Methodology is consist of required steps to improve the difference between reflectance from other seabed classes by removing path radiance, water surface reflectance and correcting the effects of water column which will result in a more accurate map of seagrass distribution.

Losinj Island is covered by four scenes of Geoeye-1 satellite images. The images were received in tiff format but converted to img format, bands of each scene were stacked together to make RGB color images and the statistics and pyramid layers were built for each scene before further analysis.

The images were already geometrically corrected and were projected to UTM 33N with WGS84 as both its datum and spheroid. Because of the lack of any large scale topographic maps or high resolution satellite images with a known RMSE error, image registration was skipped and the default registration and map projection by Digital Globe Company were accepted.

### ***3.2 method one***

#### ***3.2.1 Atmospheric correction***

Atmospheric gases, aerosols and clouds attenuate the intensity and composition of both the solar radiation and reflected radiation from the earth through scattering and absorption. Therefore, it makes atmospheric correction an essential part of processing in applications concerning the quantitative studies of the spectral characteristics of the earth surface.

This study used two different models to estimate and remove the contribution of atmosphere to the at sensor measured signal. No atmospheric measurements were available to describe the scene specific atmospheric conditions at the time of image acquisition so the extracted parameters from image metadata were modeled based on the atmospheric profile of the MODTRAN 4 radiative transfer model both in ENVI FLAASH and ERDAS IMAGINE ATCOR modules.

##### ***3.2.2.1 FLAASH***

FLAASH is designed to work with both multispectral and hyperspectral data but it gives the best results when applied for atmospheric correction of hyperspectral data. Before using the FLASH algorithm all images must be converted to a radiometrically calibrated radiance image in BIP or BIL format which was done based on the gain and bias coefficients provided in metadata.

Table 3.1) Gain and bias coefficients for Geoeye-1 satellite imagery

Band	Gain ( $\mu\text{w}/(\text{cm}^2 * \text{nm} * \text{sr})$ )	Offset
Blue	0.014865	0
Green	0.017183	0
Red	0.016194	0
NIR	0.009593	0

Input parameters of the FLAASH module is shown in table 3.1 and the result for one of the scenes can be seen in figure 3.1.

Table 3.2) input parameters of FLAASH module for all the scenes

Parameters	Scene 0000001	Scene 0010001	Scene 0010002	Scene 0020001
<b>Scene central location</b>	44.67149722 (Lat) 14.35408333 (Lon)	44.55809722 14.40438056	44.50857778 14.51917500	44.46188611 14.52225278
<b>Sensor type</b>	Geoeye-1	Geoeye-1	Geoeye-1	Geoeye-1
<b>Sensor Altitude (km)</b>	648	648	648	648
<b>Ground Elevation (km)</b>	0.1	0.06	0.45	0.30
<b>Flight date</b>	2011/07/10	2011/08/20	2011/08/20	2011/08/31
<b>Flight time GMT</b>	10:06	10:00	10:00	10:00
<b>Pixel size (m)</b>	2	2	2	2
<b>Atmospheric Model</b>	Mid-Latitude Summer	Mid-Latitude Summer	Mid-Latitude Summer	Mid-Latitude Summer
<b>Aerosol Model</b>	Maritime	Maritime	Maritime	Maritime
<b>Aerosol Retrieval</b>	None	None	None	None
<b>Water Column Multiplier</b>	1	1	1	1
<b>Initial Visibility (km)</b>	60	40	40	60

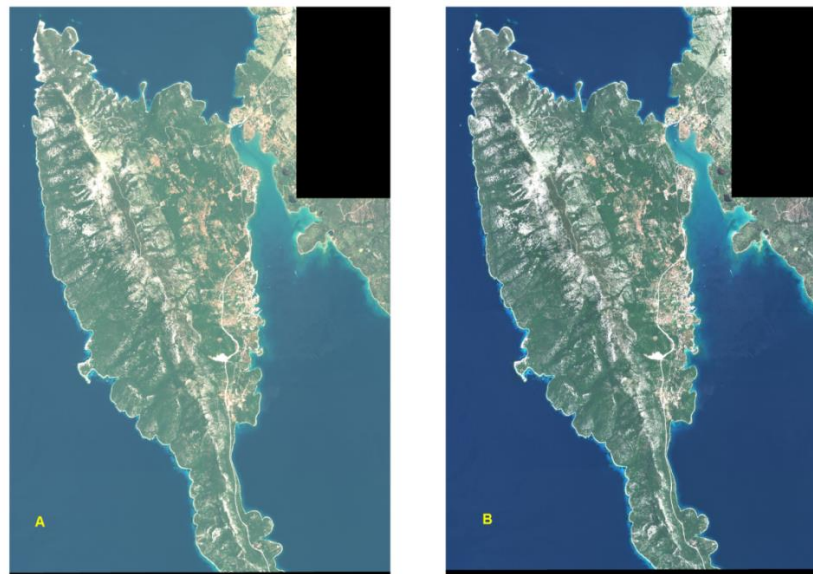


Figure 3.1) Scene 0000001 before (A) and after atmospheric correction with FLAASH (B)

### 3.2.2.2 ATCOR

ATCOR 2 atmospheric correction algorithm which is most suitable for flat terrain areas was applied to each original image scene. Unlike FLAASH, ATCOR performs radiance conversion as part of its algorithm but it needs a sensor calibration file to do the conversion.

Calibration information is available in the metadata of the imagery provided by Digital Globe. Other required inputs and their corresponding values can be found in table 3.2.

Table 3.3) input parameters of ATCOR 2 module for all the scenes

Parameters	Scene 0000001	Scene 0010001	Scene 0010002	Scene 0020001
Acquisition Date	2011/07/10	2011/08/20	2011/08/20	2011/08/31
Sensor	Geoeye-1	Geoeye-1	Geoeye-1	Geoeye-1
Calibration file	Geoeye.cal	Geoeye.cal	Geoeye.cal	Geoeye.cal
Solar Zenith	25.68279	34.96368	34.96368	38.12639
Sensor Tilt	24.33328	19.73519	19.73519	22.05353
Solar Azimuth	145.8936	151.4109	151.4109	154.9375
Satellite Azimuth	30	30	30	30
Elevation	0.1	0.06	0.45	0.30
Scene Visibility (km)	59	39	39	59
Model for solar region	Maritime midlat-summer-marit	Maritime midlat-summer-marit	Maritime midlat-summer-marit	Maritime midlat-summer-marit

Solar azimuth is directly provided in the metadata of Geoeye-1 imagery. The rest of the geometric parameters can be calculated by the following formulas based on the sensor geometric document of ATCOR for Geoeye-1 satellite imagery.

Solar zenith = 90 - Sun angle elevation

Sensor tilt = 90 – Nominal collection elevation

Satellite azimuth = Nominal collection azimuth – sun angle azimuth

Then all the angles will be rounded to the nearest define angle base on the main four direction.

S = 0°, E = 30°, N = 120° and W = 150°

Among the parameters for both modules scene (initial) visibility is the only one that cannot be obtained from the image metadata and needs additional meteorological data. It refers to the ability to distinguish a black object against a white background and its value becomes more important in the correction algorithm when the aerosol can not being retrieved.

ATCOR module has the ability to estimate the visibility value by checking dark pixels values like vegetation and water in red and NIR bands respectively and considering the lower bound as the visibility value. Also the chosen visibility can be edited repeatedly in the Spectra module to find the optimal value.

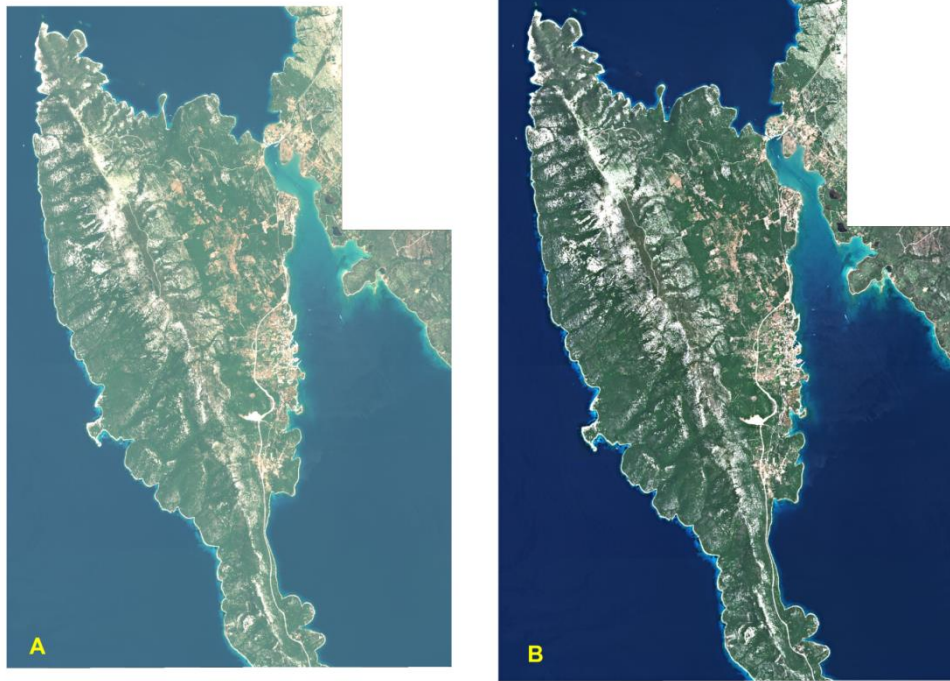


Figure 3.2) Scene 0000001 before (A) and after (B) atmospheric correction using ATCOR module

Among the two atmospheric correction modules, results from the ATCOR were chosen for further analysis. It's because of the better contrast of ATCOR in comparison to FLAASH based on the visual inspection of both images and their equivalent histogram and its ability to check for the negative values in the in the measured spectra.

### **3.2.2 Masking**

Sun glint and water depth correction are statistical analysis which are applicable only on substrate data and make incorrect result for any land areas in the image. Thus the aim of land masking is to only consider the areas of interest which are water pixels. The masked areas (land, boats) are removed from the imagery and water pixels will remain having their original values.

The process of masking follows these steps:

1- Select land and boat pixels in the image. This can be done either through a cumbersome procedure of digitizing land pixels or applying a threshold value on the image to select pixels values that belong to land areas and boats.

After exploring both the image histogram in the NIR band and some individual pixels, pixel value of 200 was chose to separate water pixels from the land pixels and the procedure was done through the function below in spatial modeler of ERDAS 2011.

EITHER 1 IF (\$n1\_atcor\_0000001 (4)>200) OR 0 OTHERWISE

2- Step 1 will result in a raster layer containing land and boat pixels. Then this raster file was converted to shapefile.

3- Then the mask shapefile was edited in ArcGIS 10.0 to remove some isolated pixels and holes in the land polygons by using first the union and then eliminate functions. Then by applying the dissolve operation a single polygon containing all the land pixels was generated.



Figure 3.3) raster threshold mask converted to shapefile (A), and then manually edited to remove isolated water pixels that incorrectly categorized as land (B) and the final result after applying union, eliminate and dissolve operations orderly (C).



- 4- Then the edited shapefile is converted back to an aoi file in ERDAS.
- 5- The aoi was used to subset the land mass from the whole image.



Figure 3.4) subset of land mass and boats from image 0000001

6- The whole image and the land mass subset were used as an input in a model with the function below to remove the land from the image and have the water pixels left.  
EITHER 0 IF (\$n2\_land) OR (\$n1\_atcor\_0000001) OTHERWISE

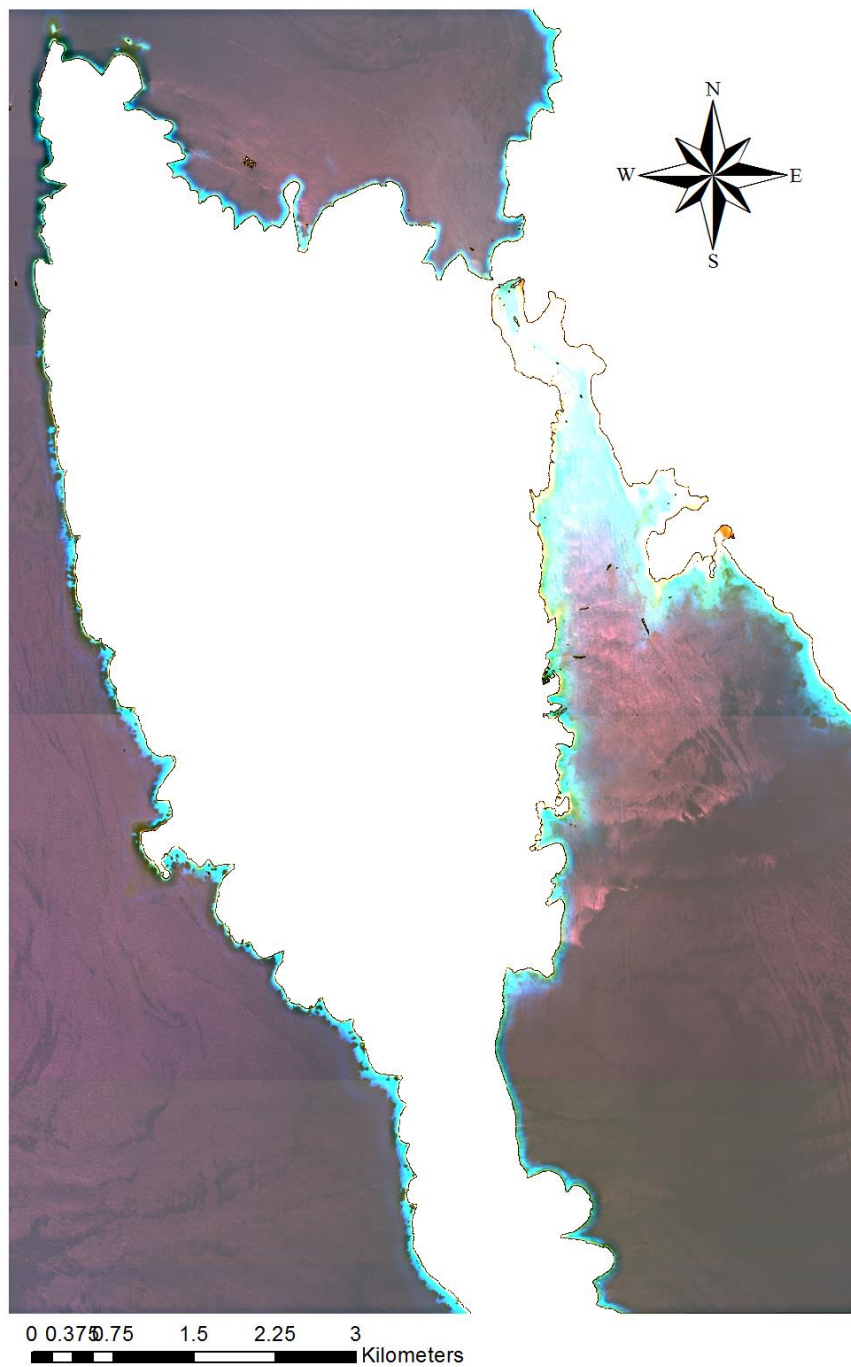


Figure 3.5) final result of masking land and boat areas.

### 3.2.3 Sun glint removal

Large percentage of coastal shallow waters often suffer from the effects of reflected light from the crests and slopes of sea surface waves that compromise the identification of benthic features.

Hedley, et al. (2005) method was used to de-glint Geoeye-1 satellite imagery scenes based on equation 7 in the second chapter. The following steps will outline the process.

- Some samples showing a range of sun glint were chosen over the optically deep water using the aoi tool in ERDAS. This step was applied on the ATCOR atmospherically corrected and masked image.
- The samples were converted to ASCII file format and opened for further analysis in EXCEL.
- Three linear regressions were performed on the pixel values of different bands: Blue vs. NIR, Green vs. NIR and Red vs. NIR. For illustration purposes the results for scene 0000001 is shown in figure 3.6.

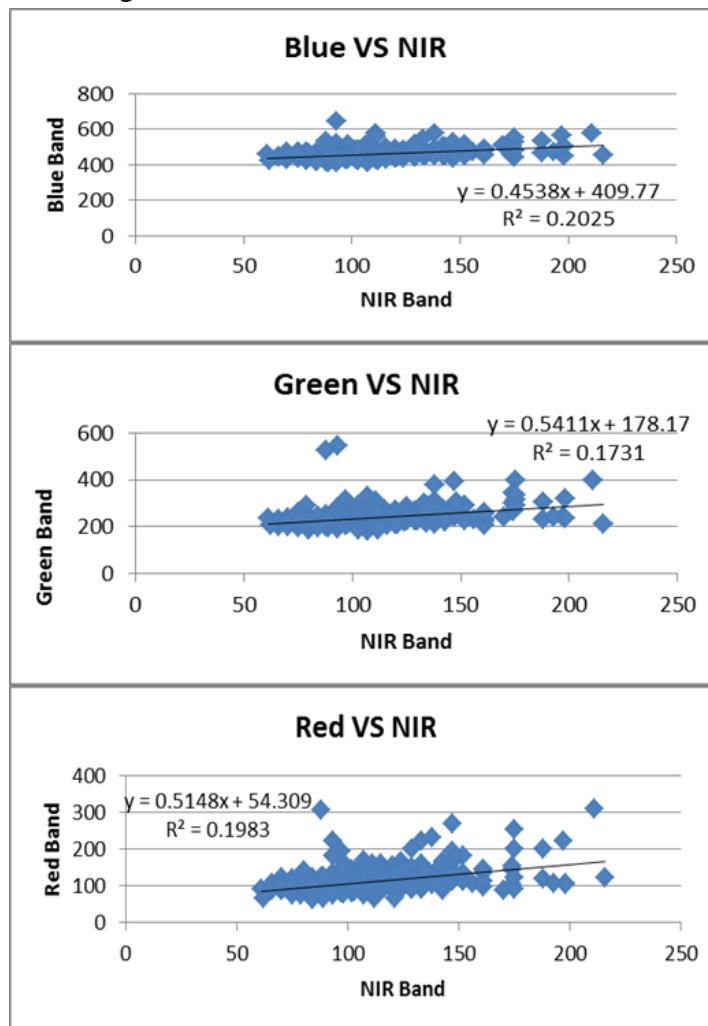


Figure 3.6) linear regression of the glint samples between different band pairs which are converted to reflectance values ( $\mu\text{w}/(\text{cm}^2 * \text{nm} * \text{sr})$ ).

- d) After calculation of the required parameters, model builder of ERDAS was used to apply equation 7 without the  $Min_{NIR}$  on the images and produce a de-glint image. Subtracting the minimum NIR value was removed because its purpose is to do a crude linear atmospheric correction but the images were already atmospherically corrected.

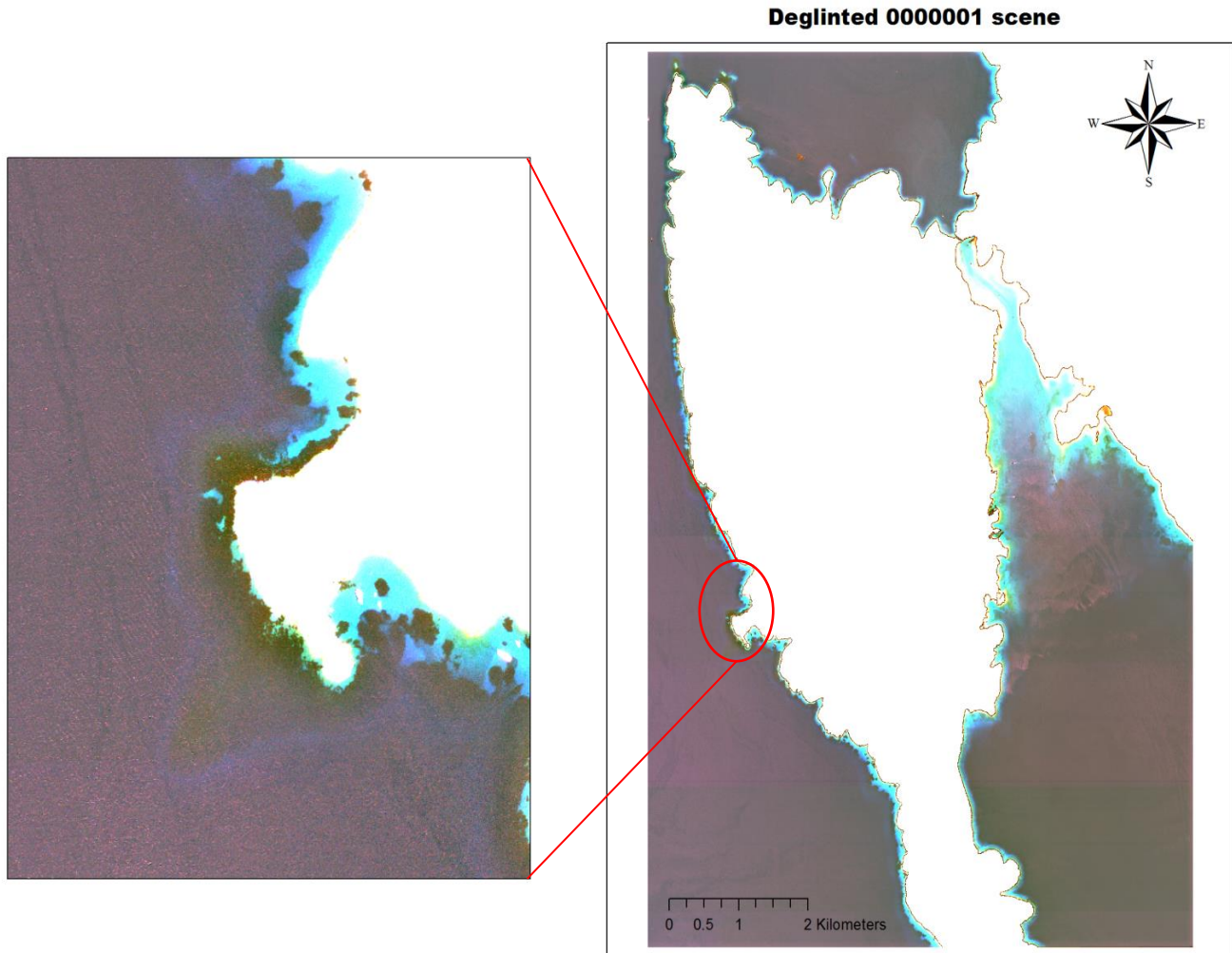


Figure 3.7) Scene 0000001 after glint correction.

### ***3.2.4 Water column correction***

As discussed in chapter 2, water column attenuate the reflected light from the sea floor features and therefore changing their reflectance which will cause problems in selecting reliable training signatures for the required classes.

To solve the problem the water column correction developed by Lyzenga (1981) was applied on the de-glinted and atmospherically corrected Geoeye-1 images which were masked for any land and boat pixels.

The correction was performed using the following steps.

- a) Samples of sand pixels from different depths were chosen from multiple locations in all image scenes using the aoi tool in ERDAS. The reason behind choosing sand to calculate the depth invariant index was the ease to recognize it in different depths without prior knowledge.
- b) The pixel values of each scene then converted to ASCII format and imported to EXCEL for further analysis.
- c) In EXCEL first, natural logarithm of pixel values for each band in each scene was calculated. Then by applying equations 13, 12 and 11 respectively on the sample data, the attenuation coefficient for each pair of bands (Blue vs. Green, Blue vs. Red and Green vs. Red) for all scenes was calculated.
- d) At last Model builder of ERDAS was used to apply equation 15 on band pairs of each scene to produce water column corrected bands.
- e) Then bands were stacked together to make a false color composite (figure 3.8).

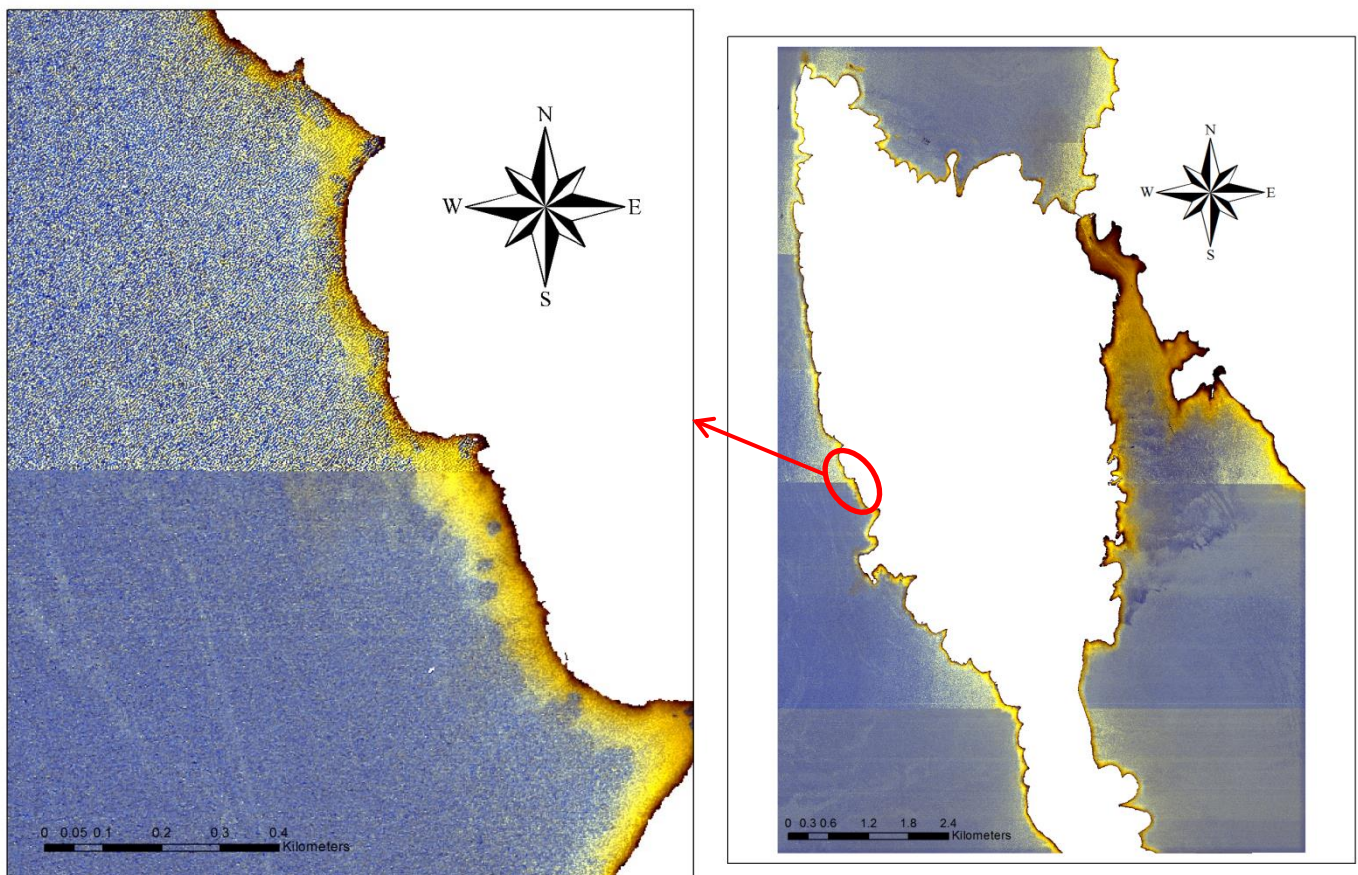


Figure 3.8) Scene 0000001 after water column correction.

### **3.3 Method two**

#### **3.3.1 Principle component analysis**

Unfortunately the original Geoeye-1 imagery contained some unidentified quality problems most probably due to erroneous sensor calibration. The noise can be seen as very big strips in all the bands which caused in very low correlation between bands. These errors prevent the statistical algorithms of method one to generate an acceptable result which can be seen in the result of de-glinting and water column correction in previous sections.

To reduce the effects of these errors (noises) and improve the spectral separability of benthic features an unstandardized PCA was applied on the atmospherically corrected images to redistribute the pixels based on eigenvectors and eigenvalues. Then, PCA1 containing 79.75% of the variability of the data was chosen and combined with the original atmospherically corrected data to make a false colour composite.



Figure 3.9) Scene 0000001 RGB: PCA1, Green, Blue

### 3.3.2 Classification

Supervised classification is applied to the combination of PCA1 and visible bands for each scene to determine different classes based on the spectral response of the training samples. A total of 200 points were selected for all the habitat classes at different depths.

And to compensate the effect of water column, each training sample with a class was considered as an individual subclass. After completing the classification for each scene, all the individual subclasses were reclassified into the main classes of the classification schema.

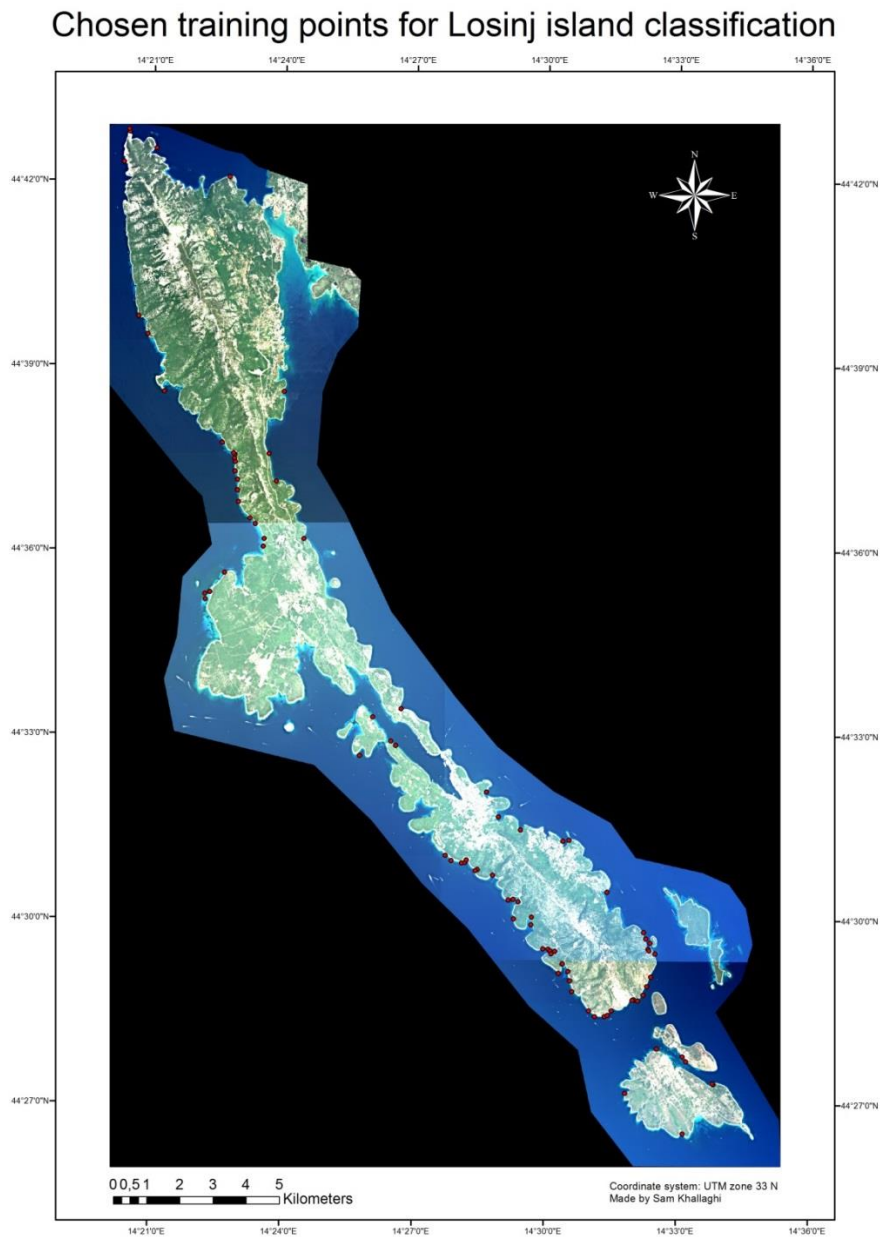


Figure 3.10) Chosen training points to train the supervised classifier

Different classification methods were tested and the best results with clear delineation of benthic features were obtained with maximum likelihood classifier. The classes used for classification are deep water, sand, rock, seagrass (*P. Oceanica*) and land.

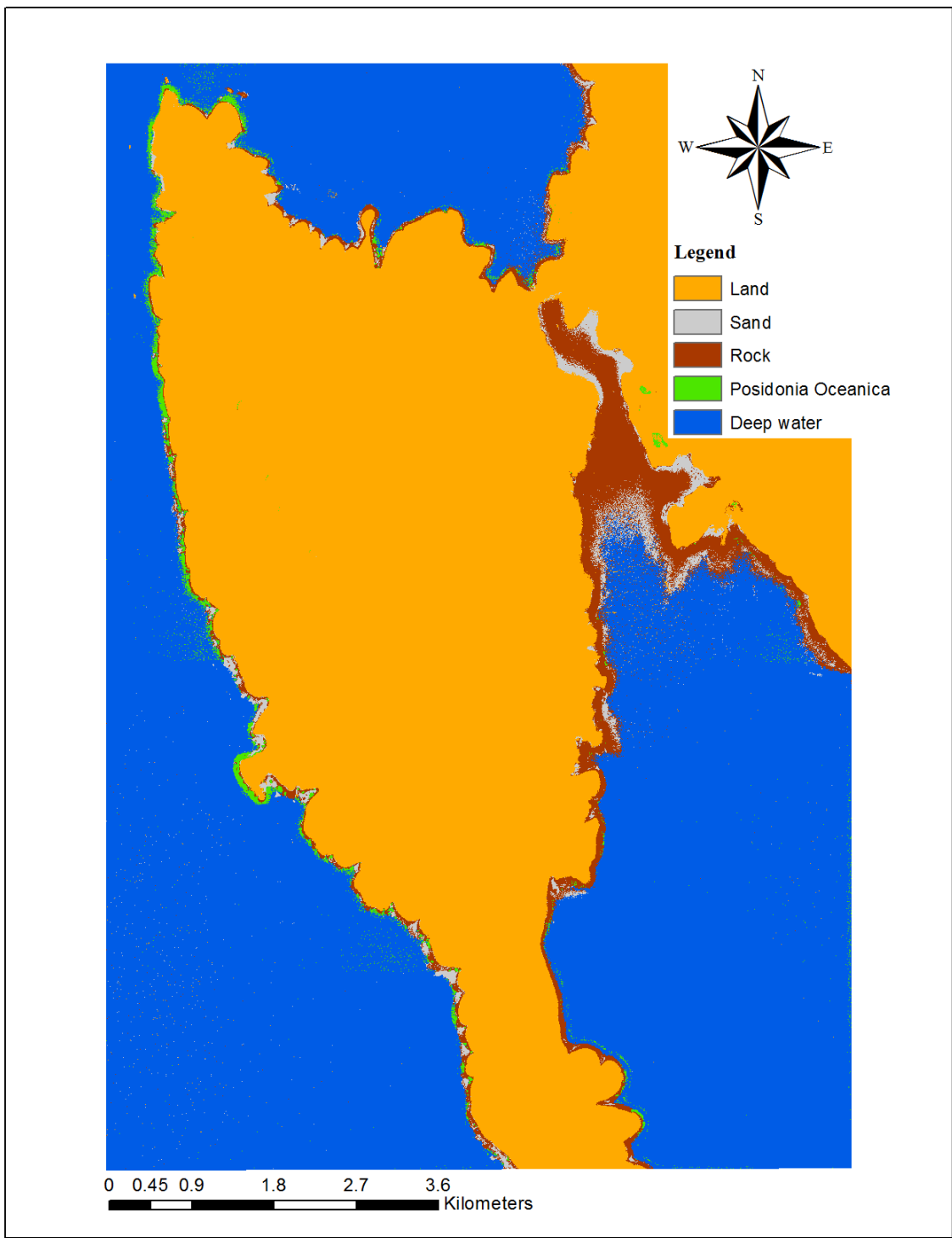


Figure 3.11) Maximum likelihood classifier results for scene 0000001



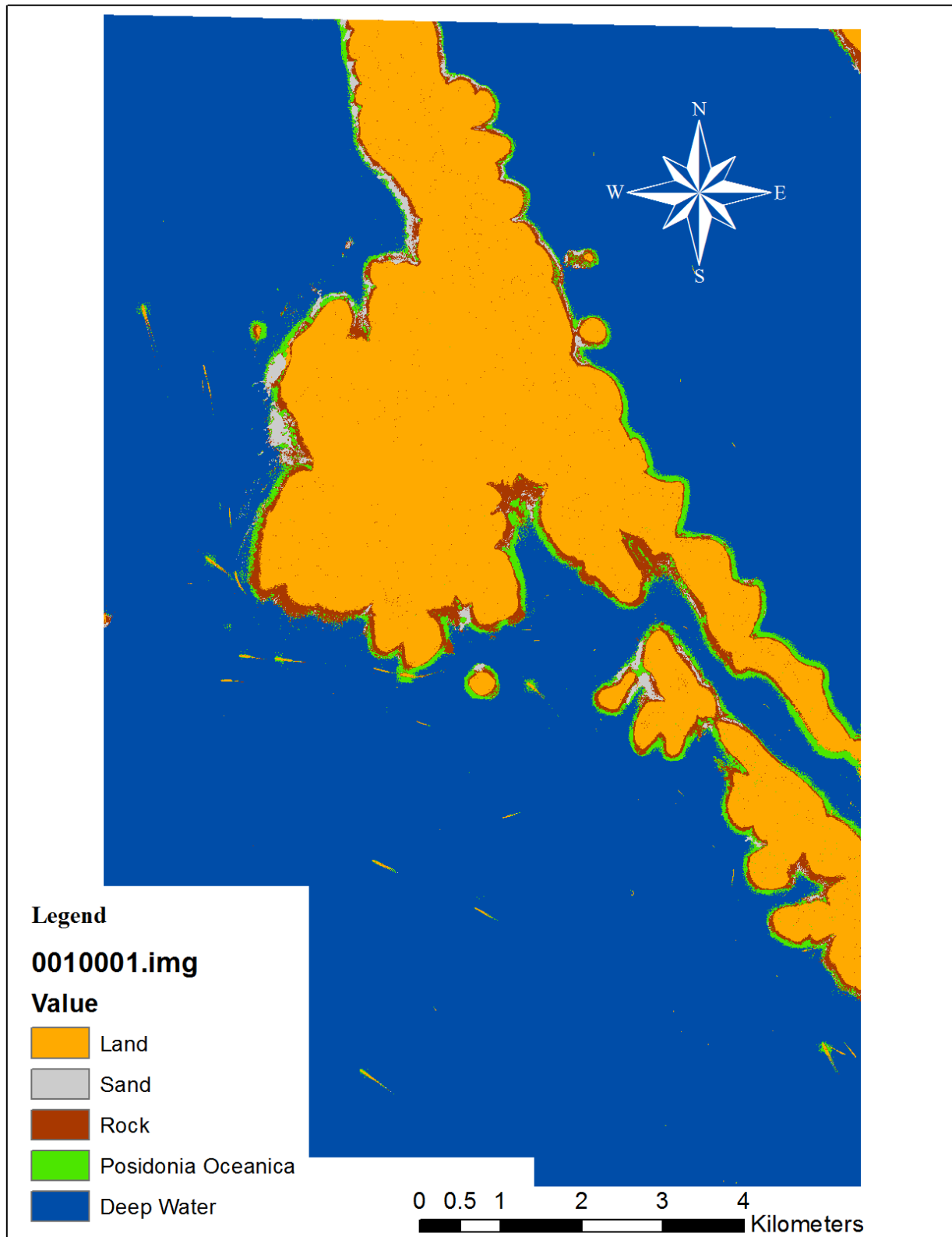


Figure 3.12) Maximum likelihood classifier results for scene 0010001

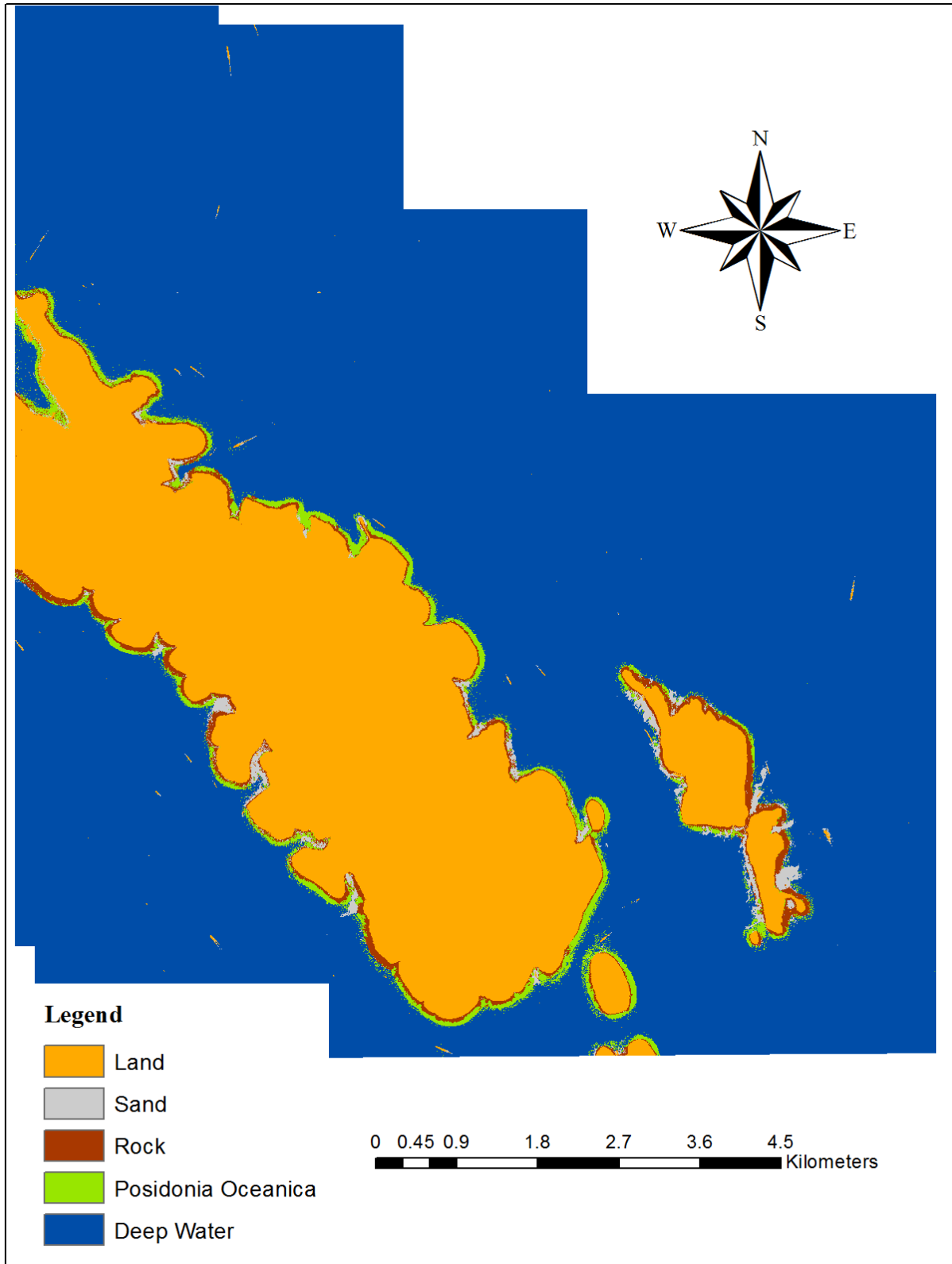


Figure 3.13) Maximum likelihood classifier results for scene 0010002

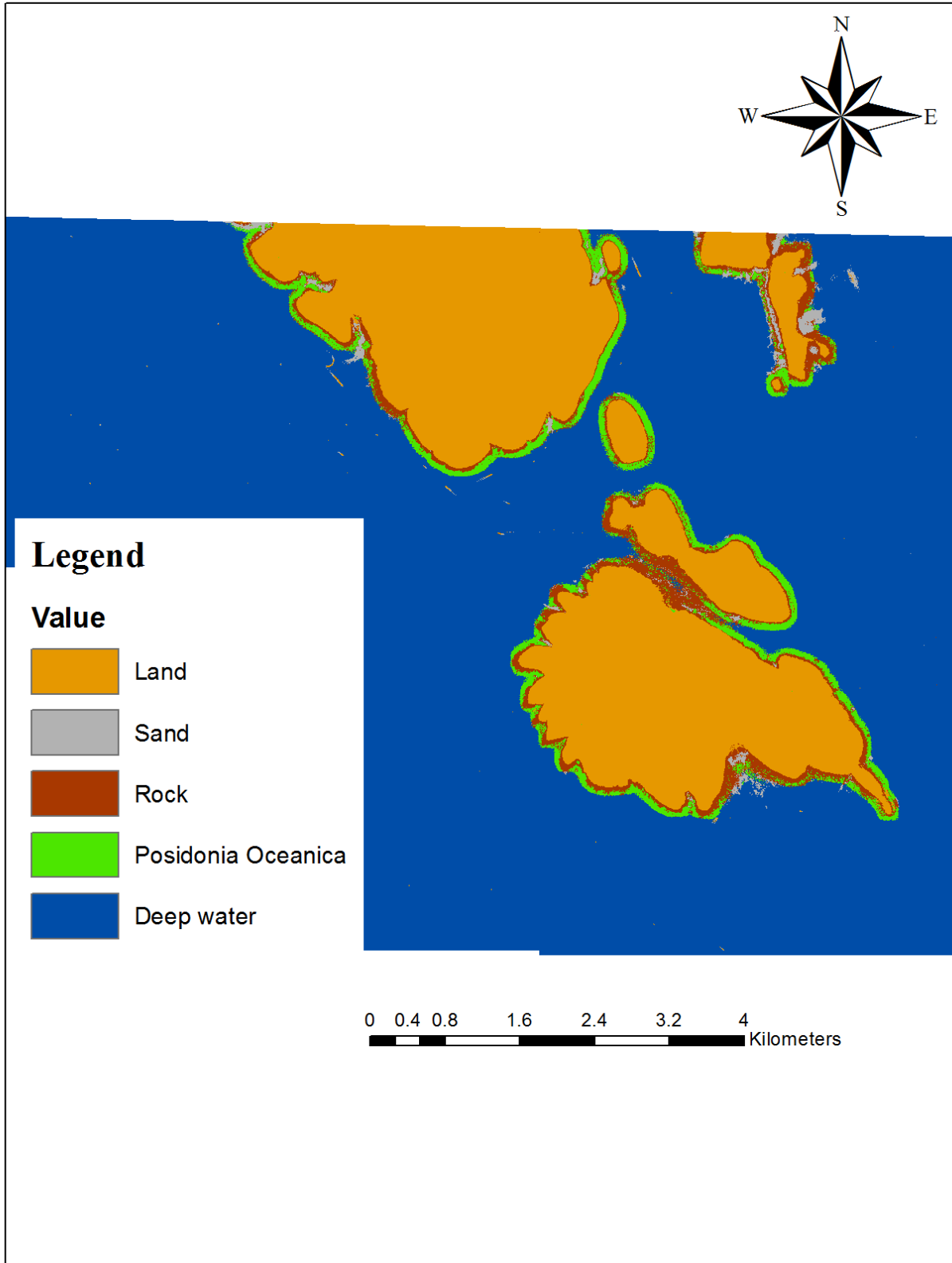


Figure 3.14) Maximum likelihood classifier results for scene 0020001

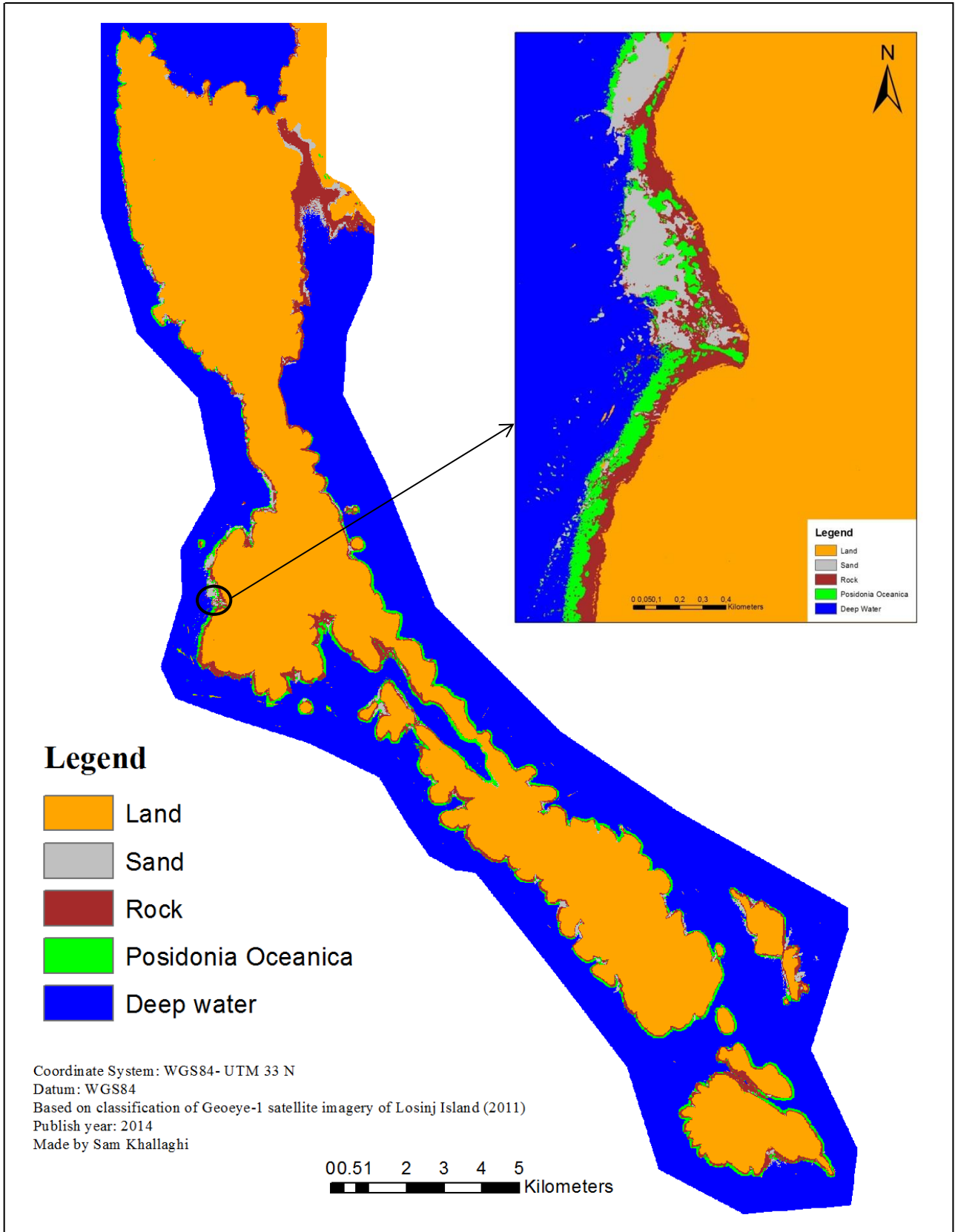


Figure 3.15) Mosaic of the edited classification result to cover whole Losinj Island

## Chapter 4 – Discussion and conclusion

### 4.1 Discussion

One of the most common methods to measure the accuracy of the classified remote sensing data is to generate the error matrix. Error matrix is comparing the classes of the result map with true reference classes which are usually obtained through field observations and assumed to have high accuracies. By applying the sea truth data of total 340 points, independent of the training samples, the habitat map was evaluated for its accuracy over sand, rock and Posidonia Oceanica. Due to the lack of sea truth data, Deep water and Land classes were omitted from the accuracy report. Measures of kappa coefficient, total, user's, producer's accuracies were derived from the error matrixes of each scene and are shown in table 4.1

Table 4.1) Classification accuracy assessment report: Derived measures from Error Matrix for all scenes and the mosaic of scenes

Image	Class Name	Producers Accuracy	Users Accuracy	Conditional Kappa	Overall Accuracy	Overall Kappa
0000001	Sand	90%	85.71%	0.8032	83.56%	0.7576
	Rock	86.96%	80%	0.7080		
	Posidonia	76.67%	95.83%	0.9293		
0010001	Sand	60.38%	96.97%	0.9536	74.51%	0.6272
	Rock	88.10%	55.22%	0.3828		
	Posidonia	77.59%	91.84%	0.8685		
0010002	Sand	90.91%	76.92%	0.7073	84.62%	0.7635
	Rock	83.33%	78.95%	0.6780		
	Posidonia	82.61%	95%	0.9103		
0020001	Sand	83.33%	83.33%	0.8155	79.03%	0.6356
	Rock	80.95%	65.38%	0.4765		
	Posidonia	77.14%	90%	0.7704		
Mosaic	Sand	72.83%	93.06%	0.9051	80.17	0.70
	Rock	81.48%	68.75%	0.5439		
	Posidonia	83.92%	88.24%	0.7982		

Inspection of table 4.1 reveals that seagrass beds are classified very accurately (more than 90% user accuracy in all the scenes). Providing that an overall accuracy of 70% and Kappa coefficient of 0.6 is acceptable, the classification result of all the scenes could be considered satisfactory. The user's accuracy showed a little decrease in the mosaic of the scenes but still it's above the acceptable range. However this is a coarse level classification with just identifying the only major seagrass species in the study area and ignoring the patchiness of the seagrass beds. So following a more detailed classification schema to identify different species and the percentage cover of the patches might not even be possible without considering the required preprocessing steps.

Although to do a thorough accuracy test, a big set of sufficient field observation over all the homogeneous substrates is a necessity. Using insufficient field observations with poor distribution might seriously affect the accuracy estimation results. For instance, in scene 0000001 the sea bed between Losinj and Cres Islands is incorrectly classified as rocky bed because of the spectral confusion between probable muddy shallow water and the rock signature and due to the lack of field data for this specific area, this big misclassification was not included in the accuracy report. Based on the visual inspection and talking to the local group that took the GPS recordings, the area is mostly made of sandy beds.

According to the literature, spectral resolution becomes extremely important in detailed level classification (>10 submerged habitat classes) and a sensor like GEOeye-1 with few broad band might not be able to spectrally discriminate similar habitats with very accurate results. However the high spatial resolution of GEOeye-1 that is usually less than the size of many habitat patches enable this sensor to map the boundary of seabed patches with better accuracy than most of sensors with better spectral resolution. This ability makes this sensor ideal for the primary studies which are just interested in the accurate boundary of the seagrass class for instance to allow the permission for building a new recreational pier based on the legal distance to the seabed patches or areas with just one major seagrass species like this research. This ability also will become even more important in Change detection studies where measuring changes in location and boundary of patches is the main concern.

Another main problem of classifying benthic habitats is the spectral similarity between bottom types. This problem even gets more complicated considering the effects of atmosphere and water column. Unfortunately the conventional statistical methods to compensate the effects of water surface reflectance and water column attenuation applied on the imagery was unsuccessful due to the quality problem inherited in the raw imagery data obtained from Digital globe Company (as discussed in section ...). The source of the error is not identified but most probably it's because of sensor calibration errors which caused very wide strip lines in all the processed scenes (figure 3.8). This caused a strangely low correlation among the visible bands and the NIR band and made all the analyses based on the regression of these bands produces unexpected results.

Table 4.2 shows the separability analysis of merged signatures of training samples for each pair of sea bottom types. It seems that the high inter class variance caused by water column attenuation would decrease the Euclidian distance between cluster centers especially for land & rock and deep water & seagrass classes. A major consequence would be the big overlapping of class signatures in the feature space which will reduce the ability of the classifier algorithm to correctly assign each pixel to its corresponding class.

Table 4.2) Average separability among the cluster center of class pairs in the merged training sample signature

Class Pairs	Best Average Separability	
1: 2	15228	1: Land 2: Sand 3: Rock 4: Posidonia Oceanica 5: Deep water
1: 3	870	
1: 4	10299	
1: 5	5555	
2: 3	14368	
2: 4	4962	
2: 5	9680	
3: 4	9444	
3: 5	4700	
4: 5	2745	

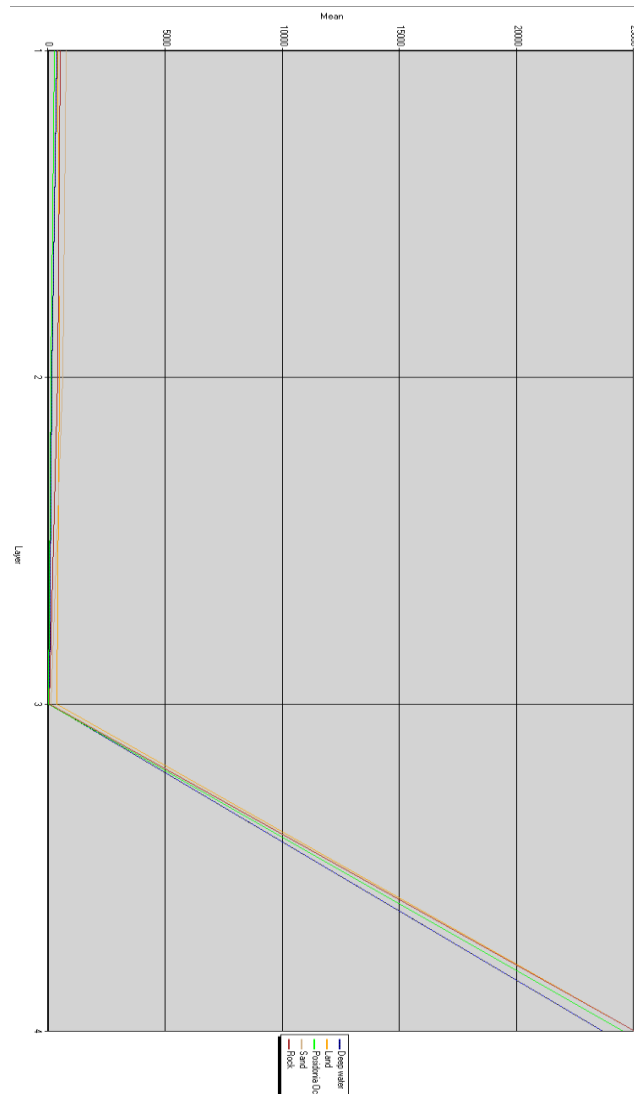


Figure 4.1) Plot of signature separability for merged training signatures for different bands (Band 1: Blue, Band 2: Green, Band 3: Red, Band 4: PCA-1) used in ML classifier.

Besides, plotting the spectral separability of training signature for the four used bands shows that the highest separability of signatures is in the fourth band (PCA1). It's obvious from figure 4.1 that the spectral separability of signatures get smaller toward the red band but becomes more distinct in the PCA1 band specially between seagrass and deep water which are very hard to draw a boundary between them even in visual inspection of the datasets. This justifies using the PCA-1 band in the classification.

To overcome the problem of water column attenuation and reduce the inner variance of the training samples for each bottom type it was decided to make several subclasses for each bottom type. The best way would be to group training samples of each class based on elevation data but because of the lack of accurate bathymetric data, each training sample were considered as a separate class and afterwards the subclasses were merged to a single parent class. Using this solution reduced the spectral overlap of training samples and improved the classification result dramatically. However based on the error matrices in appendix B, the biggest confusion can be seen between rock and Posidonia classes with the strongest overlap in scene 0020001. Most probably it's because those rocks are covered with algae or very sparse seagrass species.

## ***4.2 Conclusion and future work***

The near-shore environment around Losinj Island is complex with rocky, sandy and seagrass bottom types in different sizes and depths. The results of this study indicate that despite the spectral limitation of Geoeye-1 data, a seagrass distribution map can be produced with a reasonable accuracy using this high spatial resolution satellite imagery. Although it's important to notice that the lack of other seagrass species in the study area reduced the spectral separability problems in the classification analysis considerably and improved the accuracy of the results.

The main limiting factors in benthic habitat mapping are water turbidity, cloud cover and depth. In this study only the depth factor was the main concern especially that calculating the depth invariant index was unsuccessful for the dataset. So each training sample for a certain class was treated as an individual class and the areas that were too deep to be distinguished spectrally were classified as deep water.

This research provides the baseline for future benthic habitat studies in Croatian Islands. The data and methods used in this study can be used to assist other researchers in the selection of appropriate techniques and sensors to produce high quality, cost effective benthic maps.

For instance, it would be interesting to use both high spatial and high spectral image datasets by integrating them in a knowledge-based classification system. Or to compare the results of sun-glint removed and depth invariant datasets with the results from just atmospherically corrected datasets that are gone through textural editing, used the power of fuzzy evolutionary algorithms or object-



based methods to improve their classification results. Also besides the spatial extent of the seagrass it would be nice to estimate the biomass of the seagrass species.

## References:

- Aaby, A.A. (2004). Testing the ArcGIS Marine Data Model: Using Spatial Information to Examine Habitat Utilization Patterns of Reef Fish along the West Coast of Hawaii. MA Thesis. Oregon State University.
- Arce J.A. (2005). Remote sensing of benthic habitats in southwestern Puerto Rico. MA Thesis. University of Puerto Rico
- Arledge, R. K., Hatcher, E. B. (2008). Investigating the Effects of Higher Spatial Resolution on Benthic Classification Accuracy at Midway Atoll. MA Thesis. Naval Postgraduate School. Publication No. 0704-0188.
- Bostrom, K.J (2011). Testing the Limits of Hyperspectral Airborne Remote Sensing by Mapping Eelgrass in Elkhorn Slough. MA Thesis. University of Connecticut.
- Callaghan, A., Leeuw, G., Cohen, L., O'Dowd, C.D.. (2008). Relationship of oceanic whitecap coverage to wind speed and wind history. *Geophysical research letters*. 35, (doi:10.1029/2008GL036165).
- Chander, G., Markham, B.L., Helder, D.L.. (2009). Summary of current radiometric calibration coefficients for Landsat MSS, TM, ETM+, and EO-1 ALI sensors. *Remote Sensing of Environment*. 113, 893 – 903.
- Chavez, P. S., Jr. (1989). “Radiometric calibration of Landsat Thematic Mapper multispectral images.” *Photogrammetric Engineering and Remote Sensing* 55(9): 1285-1294.
- congallon, R.G.. (1991). A review of assessing the accuracy of classification of remotely sensed data. *Remote Sensing of Environment*. 37, 35-46.
- Curran, R.W. (2011). The Utility of Digital Globe’s WorldView-2 Satellite Data in Mapping Seagrass in North Carolina Estuaries. MA Thesis. East Carolina University.
- Cushman-Roisin, B., Gačić, M., Poulain, P-M., Artegiani, A (2002). *Physical oceanography of the Adriatic Sea*. Springer. ISBN 978-1-4020-0225-0. Retrieved 26 January 2012.
- Das, R.P. Principal component analysis in multispectral satellite images.
- Deidda, M.,Sanna, G.. (2012). Pre-processing of high resolution satellite images for sea bottom classification. *Italian Journal of Remote Sensing*. 44 (1), 83-95.
- Dennison, W. C., Orth, R.J., Moore, K. A., Stevenson, J. C., Carter, V., Kollar, S., Bergstrom, P. W., Batiuk, R. A. (1993). Assessing water quality with submerged aquatic vegetation habitat requirements as barometers of Chesapeake Bay health. *Bioscience* 43(2):87-94.
- Fornes, F., Basterretxea, G., Orfila, A., Jordi, A., Alvarez, A., Tintore, J.. (2006). Mapping *Posidonia oceanica* from IKONOS. *ISPRS Journal of Photogrammetry & Remote Sensing*. 60, 315-322.
- Gao, J. (2009). *Digital Analysis of Remotely Sensed Imagery*. New York: McGraw-Hill. 497-524.

- Green E.P., Mumby P.J., Edwards A.J., Clark C.D.. (2000). Water Column Correction Techniques. In: Edwards A.J. *Remote Sensing Handbook for Tropical Coastal Management*. Paris: Unesco. Ch.8.
- Harris, P.T.. (2011). Anthropogenic threats to benthic habitats. In: Harris, P.T., Baker, E.K. seafloor geomorphology as benthic habitat. Elsevier. 39-60.
- Hedley, J.D., Harborne A.R., Mumby P.J.. (2005). Simple and robust removal of sun glint for mapping shallow-water benthos. *International Journal of Remote Sensing*. 26 (10), 2107–2112.
- Hochberg, E.J., Andrefouet, S., Tyler, M.R.. (2003). Sea surface correction of high spatial resolution Ikonos images to improve bottom mapping in near-shore environments. *Transactions on Geoscience and Remote Sensing*. 41, 1724–1729.
- Hossein, M.K. (2005). An examination of seagrass monitoring protocols as applied to two New South Wales estuarine settings. MA Thesis. Australian Catholic University.
- Jensen J.R. (1996). *Introductory digital image processing: A remote sensing perspective (Second edition)*. USA: Prentice Hall Inc.
- Karpouzli E., Malthus T., Place C., Chui A. M., Garcia M. T., Mair J.. (2003). Underwater light characterisation for correction of remotely sensed images. *International Journal of Remote Sensing*. 24 (13), 2683–2702.
- Kawishwar, P. (2007). Atmospheric correction models for retrievals of calibrated spectral profiles from Hyperion EO-1 data. MA Thesis. Twente University.
- Kay, S.B.. (2011). Radiative transfer modelling for sun glint correction in marine satellite imagery. PhD Thesis. University of Exeter.
- Kneizys, F.X. et al.. (1996). The MODTRAN 2/3 report and LOWTRAN model. Phillips laboratory, Geophysics Directorate.
- Kokko, R. (2008). Development of an atmospheric correction code for remote sensing of water quality. MA Thesis. Helsinki University of technology.
- Kuo J., McComb A.J.. (1989). Seagrass taxonomy, structure and development. In: Larkum A.W.D., McComb A.J., Shepherd J., eds. *Biology of seagrasses: a treatise on the biology of seagrasses with special reference to the Australian region*. Elsevier, The Netherlands: 6-73.
- Larkum, A.W.D., Orth R.J., Duarte C.M. (2006). *Seagrasses: Biology, Ecology and Conservation*. Netherlands: Springer. 387-408.
- Larkum, A.W.D, West, R.J. (1990). Long-term changes of seagrass meadows in Botany Bay, Australia. *Aquatic Botany* 37: 55-70.
- Leder, T.D., Ujevic, T., Cala, M. (2004). Coastline lengths and areas of islands in the Croatian part of the Adriatic Sea determined from the topographic maps at the scale of 1:25000. *Geoadria (Zadar)* 9 (1): 5–32.

- Lillesand, T.M., Kiefer, R.W., Chipman, J.W (2007). Remote sensing and image interpretation. 6th ed. Washington: Wiley.
- Lu, D. & Weng, Q.. (2007). A survey of image classification methods and techniques for improving classification performance. *International Journal of Remote Sensing*. 28(5), 823-870. DOI: 10.1080/01431160600746456.
- Markham B.L, Barker J.L. (1986). Landsat MSS and TM post calibration dynamic ranges, exoatmospheric reflectances and at-satellite temperatures, EOSAT. Landsat Technical notes, No.1, NASA/Goddard Space Flight Center: Greenbelt, MD.
- Mather, P.M. (2011). Computer Processing of Remotely-Sensed Images, An Introduction. 4th ed. West Sussex: Wiley. 280-283.
- McKenzie L.J. (2003). Guidelines for the rapid assessment of seagrass habitats in the Western Pacific. Marine Plant Ecology Group, QDPI, Northern Fisheries Centre, Cairns.
- McKenzie L.J., Campbell S.J. and Roder C.A. (2003). Seagrass-Watch: Manual for Mapping and Monitoring Seagrass Resources by Community (citizen) Volunteers. 2nd Edition. QFS, NFC, Cairns. 100pp.
- Meyer, C.A. (2008). Application of Remote Sensing Methods to Assess the Spatial Extent of the Seagrass Resource in St. Joseph Sound and Clearwater Harbor, Florida, U.S.A. MA Thesis. University of South Florida.
- Mobley, C.D.. (1994). Light and Water (San Diego, CA: Academic Press).
- Mumby P.J., Clark C.D., Green E.P., Edwards A.J.. (1998). Benefits of water column correction and contextual editing for mapping coral reefs. *International Journal of Remote Sensing*. 19 (1), 203-210.
- Image Science and Analysis Laboratory, NASA-Johnson Space Center. (2010) The Gateway to Astronaut Photography of Earth. [Online]. Available: <http://eol.jsc.nasa.gov/newsletter/RedSeaReefs.htm> (accessed November 22st 2013 4:28 PM).
- Pahlevan, N., Valadanzouj M. J., Alimohamadi A.. (2006). A quantitative comparison to water column correction techniques for benthic mapping using high spatial resolution data. *ISPRS Commission VII Mid-term Symposium "Remote Sensing, From Pixels to Processes," Enschede, the Netherlands*. p.p 286-291.
- Pergent-Martini C., Leoni V., Pasqualini V., Ardizzone G.D., Balestri E., Bedini R., Belluscio A., Belsher T., Borg J., Boudouresque C.F., Boumaza S., Bouquegneau J.-M., Buia M.C., Calvo S., Cebrian J., Charbonnel E., Cinelli F., Cossu A., Di Maida G., Dural B., Francour P., Gobert S., Lepoint G., Meinesz A., Molenaar H., Mansour H.M., Panayotidis P., Peirano A., Pergent G., Piazzzi L., Pirrotta M., Relini G., Romero J., Sanchez-Lizaso J.L., Semroud R., Shembri P., Shili A., Tomasello A., Velimirov B. (2005). Descriptors of Posidonia oceanica meadows: Use and application. *Ecological Indicators* 5(3): 213-230.
- Podger N.E., Colwell W.B., Taylor M.H.. (2011). GeoEye-1Radiance at Aperture and Planetary Reflectance, White paper notes.

- Polina, L. (2011). Seagrass mapping and monitoring along the coasts of Crete, Greece. MA Thesis. University of Twente.
- Pu, R., Bell, S., Meyer, C., Baggett, L., Zhao, Y.. (2012). Mapping and assessing seagrass along the western coast of Florida using Landsat TM and EO-1 ALI/Hyperion imagery. *Estuarine, Coastal and shelf Science*. 115, 234-245.
- Pulliza, M.T. (2004). A multi-sensor comparison for coral reef habitat mapping: A case study using a tropical patch reef environment in Biscayne national park, Florida. MA Thesis. University of Puerto Rico.
- Robinson I.S. (2010). *Discovering the Ocean from Space: The unique applications of satellite oceanography*. Berlin: Springer.
- Sagawa, T., Boisnier, E., Komatsu, T., Mustapha, K.B., Hattour, A., Kosaka, N., Miyazaki, S.. (2010). Using bottom surface reflectance to map coastal marine areas: a new application method for Lyzenga's model. *International Journal of Remote Sensing*. 31 (12), 3051-3064.
- Schowengerdt, R. A. (2007). *Remote Sensing: Models and Methods for Image Processing*. 3rd ed. San Diego: Elsevier Inc.. 338-339.
- Seruci, S. (2010). Estimation of leaves nutrient content in seagrass using spectral data: the case of *Halodule uninervis*. MA Thesis, University of Twente.
- Short, F., Carruthers, T., Dennison, W., Waycott, M. (2007). Global seagrass distribution and diversity: A bioregional model. *Journal of Experimental Marine Biology and Ecology*. 350(1-2): 3-20.
- Tanre, D., C. Deroo, P. Duhaut, M. Herman, J. J. Morcrette, J. Perbos, and P. Y. Deschamps (1990). “Description of a computer code to simulate the satellite signal in the solar spectrum: 5S code.” *International Journal of Remote Sensing* 11: 659-668.
- Tso, B., Mather, P.M. (2009). *Classification methods for remotely sensed data*. 2nd ed. New York: CRC. 69-74.
- UNESCO 1999. *Applications of Satellite and Airborne Image Data to Coastal Management*. Coastal region and small island papers 4, UNESCO, Paris, vi + 185 pp.
- Wabnitz, C.C., Andrefouet, S., Torres-Pulliza, D., Muller-Karger, F.E., Kramer, Ph. A. (2008). Regional scale seagrass habitat mapping in the Wider Caribbean region using Landsat sensors: Applications to conservation and ecology. *Remote sensing of the environment*. 112: 3455-3467.
- West, R.J. (1983). The seagrass of New South Wales estuaries and embayments. *Wetlands* 3(1): 34-44.
- Wicaksono, P.. (2012). The Effect of Sunlight on Satellite-Based Benthic Habitat Identification. *International Journal of Advanced Research in Computer and Communication Engineering*. 1 (6), 363-370.

# Appendix A- Metadata of the used Geoeye-1 imagery

## Source Image Metadata

Number of Source Images: 3  
Source Image ID: 2011071010061881603031607487  
Product Image ID: **000**  
Sensor: GeoEye-1  
Acquired Nominal GSD  
    Pan Cross Scan: 0.4808705747 meters  
    Pan Along Scan: 0.4622387588 meters  
    MS Cross Scan: 1.9234822989 meters  
    MS Along Scan: 1.8489550352 meters  
Scan Azimuth: 269.7707353658 degrees  
Scan Direction: Reverse  
Panchromatic TDI Mode: 16  
Multispectral TDI Mode13: 10  
Multispectral TDI Mode24: 6  
Camera Cal Creation DateTime: 2011-06-23 12:20:30 GMT  
Ancillary Cal Creation DateTime: 2011-04-29 21:39:10 GMT  
Gain Cal Creation DateTime: 2009-09-18 21:20:33 GMT  
Dark Offset Cal Creation DateTime: 2009-09-21 15:01:37 GMT  
Camera Cal Effective DateTime: 2049-11-30 00:00:00 GMT  
Ancillary Cal Effective DateTime: 2011-03-26 00:00:00 GMT  
Gain Cal Effective DateTime: 2009-07-29 00:00:00 GMT  
Dark Offset Cal Effective DateTime: 2009-07-29 00:00:00 GMT  
Radiometry  
    Panchromatic  
        Gain: 0.017786  
        Offset: 0.000  
    Blue  
        Gain: 0.014865  
        Offset: 0.000  
    Green  
        Gain: 0.017183  
        Offset: 0.000  
    Red  
        Gain: 0.016194  
        Offset: 0.000  
    Near Infrared  
        Gain: 0.009593  
        Offset: 0.000  
Pan Line Rate: 10000  
Nominal Collection Azimuth: 218.5643 degrees  
Nominal Collection Elevation: 65.66672 degrees  
Sun Angle Azimuth: 145.8936 degrees

Sun Angle Elevation: 64.31721 degrees  
Acquisition Date/Time: 2011-07-10 10:06 GMT  
Percent Cloud Cover: 0

-----  
Source Image ID: 2011082010000641603031602814

Product Image ID: 001

Sensor: GeoEye-1

Acquired Nominal GSD

Pan Cross Scan: 0.4617469311 meters

Pan Along Scan: 0.4315964580 meters

MS Cross Scan: 1.8469877243 meters

MS Along Scan: 1.7263858318 meters

Scan Azimuth: 272.3164766431 degrees

Scan Direction: Reverse

Panchromatic TDI Mode: 16

Multispectral TDI Mode13: 10

Multispectral TDI Mode24: 6

Camera Cal Creation DateTime: 2011-06-23 12:20:30 GMT

Ancillary Cal Creation DateTime: 2011-04-29 21:39:10 GMT

Gain Cal Creation DateTime: 2009-09-18 21:20:33 GMT

Dark Offset Cal Creation DateTime: 2009-09-21 15:01:37 GMT

Camera Cal Effective DateTime: 2049-11-30 00:00:00 GMT

Ancillary Cal Effective DateTime: 2011-03-26 00:00:00 GMT

Gain Cal Effective DateTime: 2009-07-29 00:00:00 GMT

Dark Offset Cal Effective DateTime: 2009-07-29 00:00:00 GMT

Radiometry

Panchromatic

Gain: 0.017786

Offset: 0.000

Blue

Gain: 0.014865

Offset: 0.000

Green

Gain: 0.017183

Offset: 0.000

Red

Gain: 0.016194

Offset: 0.000

Near Infrared

Gain: 0.009593

Offset: 0.000

Pan Line Rate: 10000

Nominal Collection Azimuth: 192.4352 degrees

Nominal Collection Elevation: 70.26481 degrees

Sun Angle Azimuth: 151.4109 degrees

Sun Angle Elevation: 55.03632 degrees

Acquisition Date/Time: 2011-08-20 10:00 GMT  
Percent Cloud Cover: 0

-----  
Source Image ID: 2011083110005721603031609642

Product Image ID: 002

Sensor: GeoEye-1

Acquired Nominal GSD

Pan Cross Scan: 0.4763341844 meters

Pan Along Scan: 0.4411546886 meters

MS Cross Scan: 1.9053367376 meters

MS Along Scan: 1.7646187544 meters

Scan Azimuth: 270.3075335931 degrees

Scan Direction: Reverse

Panchromatic TDI Mode: 16

Multispectral TDI Mode13: 10

Multispectral TDI Mode24: 6

Camera Cal Creation DateTime: 2011-06-23 12:20:30 GMT

Ancillary Cal Creation DateTime: 2011-04-29 21:39:10 GMT

Gain Cal Creation DateTime: 2009-09-18 21:20:33 GMT

Dark Offset Cal Creation DateTime: 2009-09-21 15:01:37 GMT

Camera Cal Effective DateTime: 2049-11-30 00:00:00 GMT

Ancillary Cal Effective DateTime: 2011-03-26 00:00:00 GMT

Gain Cal Effective DateTime: 2009-07-29 00:00:00 GMT

Dark Offset Cal Effective DateTime: 2009-07-29 00:00:00 GMT

Radiometry

Panchromatic

Gain: 0.017786

Offset: 0.000

Blue

Gain: 0.014865

Offset: 0.000

Green

Gain: 0.017183

Offset: 0.000

Red

Gain: 0.016194

Offset: 0.000

Near Infrared

Gain: 0.009593

Offset: 0.000

Pan Line Rate: 10000

Nominal Collection Azimuth: 196.9274 degrees

Nominal Collection Elevation: 67.94647 degrees

Sun Angle Azimuth: 154.9375 degrees

Sun Angle Elevation: 51.87361 degrees

Acquisition Date/Time: 2011-08-31 10:00 GMT



Percent Cloud Cover: 0

## Appendix B- Error matrix of each scene

Table 1) Classification accuracy assessment report: Error Matrix of scene 0000001

Classified Data	Unclassified	Land	Sand	Rock	Posidonia	Deep water	Row Total
Unclassified	0	0	0	0	0	0	0
Land	0	0	0	0	0	0	0
Sand	0	0	18	1	2	0	21
Rock	0	0	2	20	3	0	25
Posidonia	0	0	0	1	23	0	24
Deep water	0	0	0	1	2	0	3
Column Total	0	0	20	23	30	0	73

Table 2) Classification accuracy assessment report: Error Matrix of scene 0010001

Classified Data	Unclassified	Land	Sand	Rock	Posidonia	Deep water	Row Total
Unclassified	0	0	0	0	0	0	0
Land	0	0	0	0	0	0	0
Sand	0	0	32	1	0	0	33
Rock	0	0	21	37	9	0	67
Posidonia	0	0	0	4	45	0	49
Deep water	0	0	0	0	4	0	4
Column Total	0	0	53	42	58	0	153

Table 3) Classification accuracy assessment report: Error Matrix of scene 0010002

Classified Data	Unclassified	Land	Sand	Rock	Posidonia	Deep water	Row Total
Unclassified	0	0	0	0	0	0	0
Land	0	0	0	0	0	0	0
Sand	0	0	10	2	1	0	13
Rock	0	0	1	15	3	0	19
Posidonia	0	0	0	1	19	0	20
Deep water	0	0	0	0	0	0	0
Column Total	0	0	11	18	23	0	52

Table 4) Classification accuracy assessment report: Error Matrix of scene 0020001

Classified Data	Unclassified	Land	Sand	Rock	Posidonia	Deep water	Row Total
Unclassified	0	0	0	0	0	0	0
Land	0	0	0	0	0	0	0
Sand	0	0	5	1	0	0	6
Rock	0	0	1	17	8	0	26
Posidonia	0	0	0	3	27	0	30
Deep water	0	0	0	0	0	0	0
Column Total	0	0	6	21	35	0	62

Table 5) Classification accuracy assessment report: Error Matrix of the mosaic

Classified Data	Unclassified	Land	Sand	Rock	Posidonia	Deep water	Row Total
Unclassified	0	0	0	0	0	0	0
Land	0	0	0	0	0	0	0
Sand	0	0	67	4	1	0	72
Rock	0	0	24	88	16	0	128
Posidonia	0	0	0	16	120	0	136
Deep water	0	0	1	0	6	0	7
Column Total	0	0	92	108	143	0	343

## **Institutionen för naturgeografi och ekosystemvetenskap, Lunds Universitet.**

Student examensarbete (Seminarieuppsatser). Uppsatserna finns tillgängliga på institutionens geobibliotek, Sölvegatan 12, 223 62 LUND. Serien startade 1985. Hela listan och själva uppsatserna är även tillgängliga på LUP student papers ([www.nateko.lu.se/masterthesis](http://www.nateko.lu.se/masterthesis)) och via Geobiblioteket ([www.geobib.lu.se](http://www.geobib.lu.se))

The student thesis reports are available at the Geo-Library, Department of Physical Geography and Ecosystem Science, University of Lund, Sölvegatan 12, S-223 62 Lund, Sweden. Report series started 1985. The complete list and electronic versions are also electronic available at the LUP student papers ([www.nateko.lu.se/masterthesis](http://www.nateko.lu.se/masterthesis)) and through the Geo-library ([www.geobib.lu.se](http://www.geobib.lu.se))

- 285 Cansu Karsili (2013) Calculation of past and present water availability in the Mediterranean region and future estimates according to the Thornthwaite water-balance model
- 286 Elise Palm (2013) Finding a method for simplified biomass measurements on Sahelian grasslands
- 287 Manon Marcon (2013) Analysis of biodiversity spatial patterns across multiple taxa, in Sweden
- 288 Emma Li Johansson (2013) A multi-scale analysis of biofuel-related land acquisitions in Tanzania - with focus on Sweden as an investor
- 289 Dipa Paul Chowdhury (2013) Centennial and Millennial climate-carbon cycle feedback analysis for future anthropogenic climate change
- 290 Zhiyong Qi (2013) Geovisualization using HTML5 - A case study to improve animations of historical geographic data
- 291 Boyi Jiang (2013) GIS-based time series study of soil erosion risk using the Revised Universal Soil Loss Equation (RUSLE) model in a micro-catchment on Mount Elgon, Uganda
- 292 Sabina Berntsson & Josefin Winberg (2013) The influence of water availability on land cover and tree functionality in a small-holder farming system. A minor field study in Trans Nzoia County, NW Kenya
- 293 Camilla Blixt (2013) Vattenkvalitet - En fältstudie av skånska Säbybäcken
- 294 Mattias Spångmyr (2014) Development of an Open-Source Mobile Application for Emergency Data Collection
- 295 Hammad Javid (2013) Snowmelt and Runoff Assessment of Talas River Basin Using Remote Sensing Approach
- 296 Kirstine Skov (2014) Spatiotemporal variability in methane emission from an Arctic fen over a growing season – dynamics and driving factors
- 297 Sandra Persson (2014) Estimating leaf area index from satellite data in deciduous forests of southern Sweden
- 298 Ludvig Forslund (2014) Using digital repeat photography for monitoring the regrowth of a clear-cut area
- 299 Julia Jacobsson (2014) The Suitability of Using Landsat TM-5 Images for Estimating Chromophoric Dissolved Organic Matter in Subarctic Lakes
- 300 Johan Westin (2014) Remote sensing of deforestation along the trans-Amazonian highway

- 301 Sean Demet (2014) Modeling the evolution of wildfire: an analysis of short term  
wildfire events and their relationship to meteorological variables
- 302 Madelene Holmblad (2014). How does urban discharge affect a lake in a  
recreational area in central Sweden? – A comparison of metals in the sediments of  
three similar lakes
- 303 Sohedul Islam (2014) The effect of the freshwater-sea transition on short-term  
dissolved organic carbon bio-reactivity: the case of Baltic Sea river mouths
- 304 Mozafar Veysipanah (2014) Polynomial trends of vegetation phenology in  
Sahelian to equatorial Africa using remotely sensed time series from 1983 to 2005
- 305 Natalia Kelbus (2014) Is there new particle formation in the marine boundary  
layer of the North Sea?
- 306 Zhazhang Cai (2014) Modelling methane emissions from Arctic tundra wetlands:  
effects of fractional wetland maps
- 307 Erica Perming (2014) Paddy and banana cultivation in Sri Lanka - A study  
analysing the farmers' constraints in agriculture with focus on Sooriyawewa D.S.  
division
- 308 Nazar Jameel Khalid (2014) Urban Heat Island in Erbil City.
- 309 Jessica, Ahlgren & Sophie Rudbäck (2014) The development of GIS-usage in  
developed and undeveloped countries during 2005-2014: Tendencies, problems  
and limitations
- 310 Jenny Ahlstrand (2014) En jämförelse av två riskkarteringar av fosforförlust från  
jordbruksmark – Utförda med Ekologgruppens enkla verktyg och  
erosionsmodellen USPED
- 311 William Walker (2014) Planning Green Infrastructure Using Habitat Modelling. A  
Case Study of the Common Toad in Lomma Municipality
- 312 Christiana Marie Walcher (2014) Effects of methane and coastal erosion on  
subsea-permafrost and emissions
- 313 Anette Fast (2014) Konsekvenser av stigande havsnivå för ett kustsamhälle- en  
fallstudie av VA systemet i Beddingestrand
- 314 Maja Jensen (2014) Stubbrytningens klimatpåverkan. En studie av  
stubbrytningens kortsiktiga effekter på koldioxidbalansen i boreal barrskog
- 315 Emelie Norhagen (2014) Växternas fenologiska svar på ett förändrat klimat -  
modellering av knoppsprickning för hägg, björk och asp i Skåne
- 316 Liisi Nõgu (2014) The effects of site preparation on carbon fluxes at two clear-  
cuts in southern Sweden
- 317 Julian Will (2014) Development of an automated matching algorithm to assess the  
quality of the OpenStreetMap road network - A case study in Göteborg, Sweden
- 318 Niklas Olén (2011) Water drainage from a Swedish waste treatment facility and  
the expected effect of climate change
- 319 Wösel Thoresen (2014) Burn the forest - Let it live. Identifying potential areas for  
controlled forest fires on Gotland using Geographic Information System
- 320 Jurgen van Tiggelen (2014) Assimilation of satellite data and in-situ data for the  
improvement of global radiation maps in the Netherlands.
- 321 Sam Khallaghi (2014) Posidonia Oceanica habitat mapping in shallow coastal  
waters along Losinj Island, Croatia using Geoeye-1 multispectral imagery.